Journal of Controlled Release 352 (2022) 1116–1133

Contents lists available at ScienceDirect

Journal of Controlled Release

journal homepage: www.elsevier.com/locate/jconrel

Biomimetic photosensitizer nanocrystals trigger enhanced ferroptosis for improving cancer treatment

Mingbo Wu [a,b,1], Wenwu Ling [c,1], Jiaojun Wei [b], Ran Liao [d], Haiyue Sun [b], Dongqiu Li [b], Ye Zhao [b,*], Long Zhao [b,d,*]

[a] State Key Laboratory of Biotherapy and Cancer Center, West China Hospital, Sichuan University and Collaborative Innovation Center for Biotherapy, Chengdu 610041, PR China
[b] School of Bioscience and Technology, Chengdu Medical College, Chengdu 610500, PR China
[c] Department of Ultrasoundx, West China Hospital, Sichuan University, Chengdu 610041, PR China
[d] The Second Affiliated Hospital of Chengdu Medical College, China National Nuclear Corporation 416 Hospital, Chengdu 610051, PR China

ARTICLE INFO

Keywords:
Photodynamic therapy
Ferroptosis
Synergistic treatment
Biomimetic nanocrystals
Target recognition

ABSTRACT

As a novel non-apoptotic cell death pathway, ferroptosis can effectively enhance the antitumor effects of photodynamic therapy (PDT) by disrupting intracellular redox homeostasis. However, the reported nanocomposites that combined the PDT and ferroptosis are cumbersome to prepare, and the unfavorable tumor microenvironment also severely interferes with their tumor suppressive effects. To address this inherent barrier, this study attempted to explore photosensitizers that could activate ferroptosis pathway and found that the photosensitizer aloe-emodin (AE) could induce cellular ferroptosis based on its specific inhibiting activity to Glutathione S-transferase P1(GSTP1), a key protein for ferroptosis. Herein, we prepared AE@RBC/Fe nanocrystals (NCs) with synergistic PDT and ferroptosis therapeutic effects by one-step emulsification to obtain AE NCs cores and further modification of red blood cells (RBC) membranes and ferritin. Benefiting from the involvement of ferritin, the prepared AE@RBC/Fe NCs provide not only sufficient oxygen for oxygen-dependent PDT, but also Fe^{3+} for iron-dependent ferroptosis in tumor cells. Furthermore, the biomimetic surface functionalization facilitated the prolonged circulation and cancer targeting of AE@RBC/Fe NCs *in vivo*. The *in vitro* and *in vivo* results demonstrate that AE@RBC/Fe NCs exhibit significantly enhanced therapeutic effects for the combined two antitumor mechanisms and provide a promising prospect for achieving PDT/ferroptosis synergistic therapy.

1. Introduction

Ferroptosis is an iron-dependent programmed cell death modality, that is closely associated with the excessive accumulation of intracellular reactive oxygen species (ROS) and related lipid peroxide (LPO) [1]. Since the first introduction for the pathway of ferroptosis by Stockwell in 2012 [2], convincing evidence has suggested that the use of ferroptosis inducers can effectively suppress tumor growth [3]. To date, some well-established ferroptosis inducers have been identified. For example, Erastin can reduce glutathione (GSH) level by inhibiting the activity of the cystine/glutamate antagonist system **X- c**, and RSL3 can directly inhibit the activity of glutathione peroxidase 4 (GPX4), a specific enzyme that functioning by repairing oxidized phospholipids and/or decreasing GSH level [4]. In addition, ferroptosis is closely related to the Fenton reaction mediated by ferric ion (Fe^{3+}), which is reduced to ferrous ion (Fe^{2+}) by divalent metal transporter 1 (DMT-1) in endosomes while producing cytotoxic ROS [5]. Therefore, the application of suitable ferroptosis inducers and combined with Fe^{3+}-mediated Fenton reaction would be a promising strategy for cancer therapy.

Photodynamic therapy (PDT) is a fashionable non-invasive tumor treatment, which can be operated in restricted area with a controlled manner, and exhibits higher selectivity and lower side effects compared to conventional chemotherapy, especially in the treatment of superficial tumors [6]. However, a compromising factor for PDT is that cancer cells possess a robust oxidative defense system. Once cellular damage is induced by PDT, the over-production GSH in tumor cells would

* Corresponding author at: School of Bioscience and Technology, Chengdu Medical College, No.783 Xindu Avenue, Xindu District, Chengdu 610500, PR China.
E-mail addresses: zhaoye525@cmc.edu.cn (Y. Zhao), longzhao@cmc.edu.cn (L. Zhao).
[1] The authors contributed equally to this work.

https://doi.org/10.1016/j.jconrel.2022.11.026
Received 3 August 2022; Received in revised form 5 November 2022; Accepted 14 November 2022

counteract oxidative stress in an attempt to maintain the redox homeostasis [7]. To subtly address the obstacles, it has been reported that the Fe^{3+} in tumor cells can not only deplete GSH but also catalyze the decomposition of endogenous hydrogen peroxide (H_2O_2) to generate oxygen [8]. Therefore, it is conceivable that the synergy between the Fe^{3+} and PDT would achieve enhanced anti-tumor effects by promoting ROS production at the tumor site and disrupting the oxidative defenses of tumor cells.

Currently, common photosensitizers are mainly excited in the red region, which may produce damage to deeper normal tissues when treating superficial diseases with PDT. For example, PDT with 630 nm laser irradiation for cancer in the esophagus and bronchus may occasionally lead to wall perforations and fistulas [9]. Thus, exploring new photosensitizers with shorter excitation wavelength from existing clinical drugs will expand PDT applications. Aloe-emodin (AE) is an anthraquinone derivative extracted from traditional Chinese herbal plant that shows stable light absorption in the blue region and can be used as a new photosensitizer for PDT [10]. Previous reports have shown that AE exhibited undeniable pharmacological activity for antitumor and has proven its cytotoxic effect on a variety of cancer cells including breast cancer, pancreatic cancer, lung carcinoma, hepatocellular carcinoma and gastric carcinoma, although the exact mechanism remains to be elucidated [11]. Lu et al. found that AE can deplete intracellular GSH while leading to redox imbalance as well as sustained activation of c-Jun N-terminal kinase (JNK) inducing apoptosis [12]. Wang et al. attempted to explain the attractive result of GSH depletion by AE through a LC-MS/MS analysis system, and the result suggested that AE, an electrophilic specie, can chemically react with GSH to form specific conjugate [13]. As mentioned above, the down-regulation of GSH is responsible for cellular ferroptosis, so it's reasonable to assume that AE may also act as a potential ferroptosis inducer. But to our knowledge, there is currently no relevant studies.

In summary, AE can integrate and enhance PDT and ferroptosis simultaneously when an efficient Fe^{3+} donor is involved. Ferritin, a major intracellular iron storage protein, is composed of ferritin heavy chains (Fth) and ferritin light chains (Ftl) [14]. Recent studies indicate that intracellular degradation of ferritin can increase Fe^{3+} levels, leading to oxidative cellular damage caused by the Fenton reaction [15]. In addition, ferritin can be recognized by tumor cells in association with the overexpression of transferrin receptor 1 (TfR1) [16]. Clearly, ferritin has a natural advantage over other materials for ferroptosis and/or PDT owing to its inherent iron storage and tumor-specific recognition properties.

Oral squamous cell carcinoma is a common malignancy of the oral and maxillofacial cavity with a 5-year survival rate of only about 50% [17]. PDT can provide better functional cosmetic outcomes than traditional ablative surgery while preserving the speech and swallowing functions [18]. Although AE can act as a potential ferroptosis inducer and photosensitizer for specific surface disease, it still suffers from unfavorable pharmacokinetic characteristics. Therefore, simple and effective strategies are urgently needed to increase AE concentration in tumor cells to therapeutic threshold. Here, we first clarified the metabolic pathway of AE-induced ferroptosis, and then developed a novel ferritin-modified biomimetic AE nanocrystals (AE@RBC/Fe NCs) by co-extruding AE nanocrystals (NCs), prefabricated red blood cells (RBC) membranes and ferritin (Fe) for the synergistic treatment of PDT and ferroptosis (Scheme 1a). The AE NCs were camouflaged with ferritin-decorated RBC membranes, which enable them superior long circulation and targeting capabilities while retaining the functionality of the AE NCs core. Compared to other nanoscopic dosage forms, the current design of biomimetic NCs with colloidal stability and sustained release properties are more suitable for hydrophobic compounds like AE, allowing them to deliver almost 100% of the drug when used parenterally. Upon uptake by tumor cells, over-expressed phospholipases D (PLD) in the tumor cell could disintegrate the phospholipid component of the outer layer of AE@RBC/Fe NCs, resulting in the exposure and release of the AE NCs inner core. AE not only exerts the properties of a photosensitizer to convert intracellular oxygen to $^1O_2$ under laser irradiation, but also initiates ferroptosis by inhibiting the activity of Glutathione S-transferase P1(GSTP1). More importantly, thanks to the involvement of ferritin, both AE-mediated ferroptosis and PDT were effectively enhanced due to Fe^{3+} supply and oxygen replenishment (Scheme 1b). This work provides insight into the antitumor effects of AE@RBC/Fe NCs, and indicates that AE@RBC/Fe NCs can serve as a very promising candidate for synergistic ferroptosis and PDT in future clinical translation.

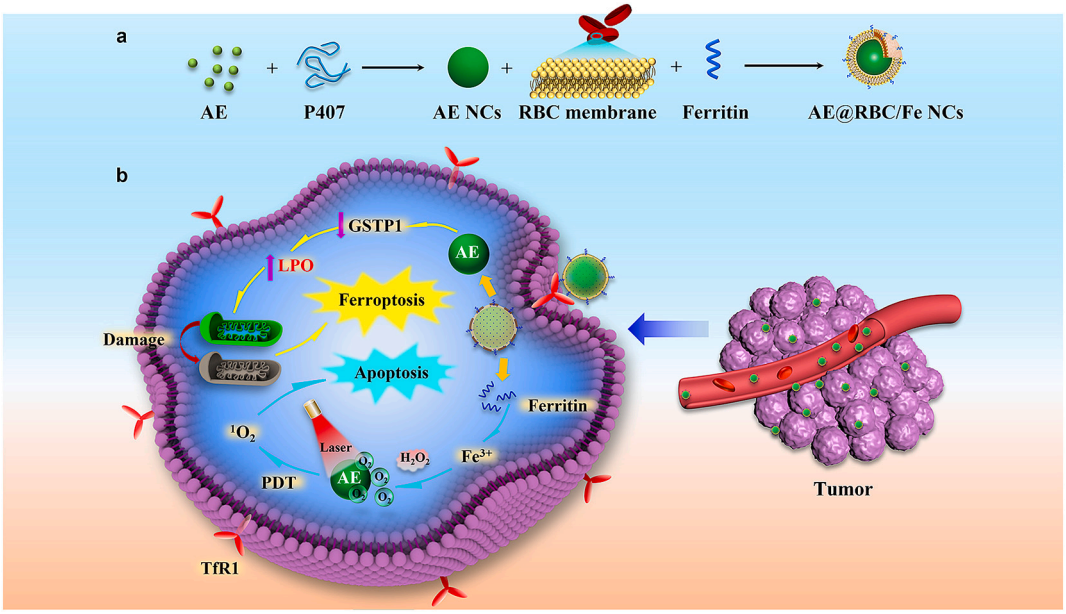

Scheme 1. (a) Preparation procedure of AE@RBC/Fe NCs. (b) Schematic illustration of PDT/ferroptosis synergistic therapy after intravenous injection of AE@RBC/Fe NCs.

2. Materials and methods

2.1. Materials

AE, 3-(4,5-dimethylthiazol-2-yl)-2,5-diphenyltetrazolium bromide (MTT), trypsin, GSH, 2′,7′-dichlorofluorescin diacetate (DCFH-DA), annexin V-FITC, propidium iodide (PI), 4′,6-diamidino-2-phenylindole (DAPI), Deferoxamine (DFO), Cyanine 5.5 (Cy5.5) and PLD (*EC* 3.1.4.4) were offered by Sigma-Aldrich (Shanghai, China). Recombinant GSTP1 protein (ab167990), anti-GPX4, anti-GSTP1, anti-JNK anti-Ki-67, anti-Caspase-3, anti-4-hydroxy-2-nonenal (4-HNE) antibody were provided by Abcam (Shanghai, China). GST activity fluorescent assay, BOD-IPY$^{581/591}$-C11 and singlet oxygen sensor green (SOSG) kit were offered by Thermo Fisher (Waltham, MA). Poloxamer-407 (P407), Ferrostatin-1 (Fer-1), Ac-DEVD-CHO (Apo) and JC-1 Mitochondrial Assay Kit were provided by Aladdin (Shanghai, China). Thiobarbituric acid reactive substances (TBARS) assay kit was purchased from Cayman Chemical. Lentiviral vectors which overexpress GSTP1 were purchased from GeneChem (Shanghai, China). All other chemicals and solvents at reagent grade or better were offered by Changzheng Regents Co. (Chengdu, China), unless otherwise explained. All cell lines in this research (human oral squamous carcinoma cells HSC-3, mouse embryonic fibroblast cells NIH 3T3) were provided by the American Type Culture Collection (ATCC, Manassas, USA) originally. Sichuan Dashuo Biotech. Inc. (Chengdu, China) offered Sprague Dawley rats and Balb/c nude mice.

2.2. Preparation of AE@RBC/Fe NCs

AE NCs were prepared based on the approach described in previous reports with slight modifications [19]. Briefly, a suitable mixture of AE (0.1 *w/v*) and P407 (0.5 w/v) was added to DMSO to fully dissolve, and then the mixture solution was intensely sonicated and continuously stirred in D. I. water (pH 4.0) for 30 min until homogeneous opaque yellow AE NCs were formed, which were subsequently separated by centrifugation. The encapsulation efficiency of AE NCs was determined by an ultraviolet-visible (UV–Vis) spectrophotometer (UV-2550, Shimadzu, Japan) with an absorption peak at 431 nm (encapsulation efficiency = 100% − [amount of AE in the remaining solution] / [total amount of AE] × 100%). Human whole blood was collected from health volunteers by our collaborators at the Second Affiliated Hospital of Chengdu Medical College with the approval of the Institutional Review Board (IRB). Fresh whole blood was withdrawn from the orbit of Sprague Dawley rats with low molecular heparin solution for anticoagulation. RBC membrane fragments were extracted from whole blood samples collected using the previously described protocol [20]. In order to decorate the NCs with ferritin while fusing RBC membrane fragments with AE NCs, the corresponding amounts of AE NCs, pre-prepared RBC membrane fragments and ferritin were mixed in the mass ratio of 1:1:2%, and then the three components were co-extruded several times through a 220 nm polycarbonate porous membrane applying an Avanti mini extruder [21]. AE@RBC/Fe NCs was subsequently separated by centrifugation washed to remove excess vesicles and proteins for further characterization. In addition, AE@RBC NCs (AE NCs and RBC membrane fragments were mixed) and RBC/Fe complex (ferritin and RBC membrane fragments were mixed) were prepared using a similar co-extrusion method as described above. The concentrations of RBC/Fe complex were quantified by bicinchoninic acid (BCA) kit.

2.3. Physico-chemical characterization of NCs

The crystallographic patterns of AE@RBC/Fe NCs and naked AE NCs were characterized by powder X-ray diffraction (PXRD; Philips X'Pert PRO, The Netherlands) applying Cu-Ka radiation source with a spectral collection range between 5° - 40° in steps of 0.05°. Morphological analysis of NCs was performed by transmission electron microscopy (TEM; FEI Tecnai F20, USA). The hydrous size and zeta potentials of NCs were measured with dynamic light scattering (DLS; Malvern Nano-ZS90, UK). The iron composition in AE@RBC/Fe NCs was quantitatively evaluated by inductively coupled plasma-optical emission spectrometry (ICP-OES, Agilent ICP-OES 7300 DV, USA). The stability of NCs in PBS was evaluated *via* measuring the particle size of NCs at different time points at room temperature.

The surface protein content of various NCs was decided with a BCA kit. In addition, sodium dodecyl sulfate-polyacrylamide gel electrophoresis (SDS-PAGE) integrated with Coomassie blue for protein staining was adopted to analyze the protein components of the different modified NCs. To identify the membrane orientation of AE@RBC/Fe NCs, the glycoprotein content of AE@RBC/Fe NCs was quantified according to a previous method [22]. Briefly, 1 mL of AE@RBC/Fe NCs (1 mg/mL) suspension was incubated with trypsin for 2 h at room temperature to initiate trypsinization. The samples were then centrifuged at 10000 rpm for 10 min, and the supernatant was collected to quantify glycoprotein using a glycoprotein ELISA Kit following the manufacturer's instructions. The ratio of full cell membrane coating was calculated by previously reported fluorescence quenching assay [23]. Briefly, AE@RBC NCs and AE@RBC/Fe NCs were prepared with fluorescent nitro-2,1,3-benzoxadiazol-4-yl (NBD)-labeled AE NCs as the core, followed by the addition of dithionite (DT) solution to the samples. The reserved fluorescence of the cell membrane-coated NCs after the addition of DT was measured by fluorescence spectrophotometer (Hitachi F-7000, Japan) to calculate ratio of full coating.

2.4. Release of AE and Fe^{3+}

The effect of PLD on the degradation and release properties of AE@RBC/Fe NCs in PBS solutions with different pH conditions was investigated. The reverse dialysis was performed by homogeneously dispersing 5 mg of AE NCs and AE@RBC/Fe NCs in 50 mL of PBS (pH 7.4 and pH 5.5) in a horizontal laboratory shaker with a rate of 100 rpm at 37 °C. Take 2.0 mL of the above sample from the dialysis bag (MWCO: 1000 Da) and the released AE in the buffer solutions was quantified by a fluorescence spectrophotometer under the excitation/emission wavelengths of 429/520 nm according to the standard calibration curve. In addition, the release profile of AE@RBC/Fe NCs in PBS containing PLD was determined by the same method. TEM was used to observe the morphological changes of AE@RBC/Fe NCs under different conditions at preset time intervals.

To confirm the involvement of Fe^{3+} from ferritin in the redox cycle, *o*-phenanthroline was used as an indicator to verify the production of Fe^{2+}. AE@RBC/Fe NCs were dispersed in a weakly acidic solution (pH 5.5) for 4 h and the color change was observed by sequential addition of *o*-phenanthroline, GSH or/and H_2O_2. The reactions of $FeCl_3$, $FeCl_2$, GSH and H_2O_2 with o-phenanthroline were used as controls, respectively.

2.5. Detection of extracellular $^1O_2$ and oxygen generation

$^1O_2$ production was detected using SOSG as a probe according to a previous report [24]. 20 μg of AE@RBC/Fe NCs were dispersed in 1 mL of a weakly acidic solution (pH 5.5) containing PLD for 1 h. Subsequently, 5 μL of SOSG methanol solution (5 mM) was added and the mixed solution was irradiated with a 405 nm laser (Oxxius LBX, France) for different times (0, 3, 6, 9 and 12 min). The fluorescence intensity of the solution was measured by a fluorescence spectrophotometer under the excitation/emission wavelengths of 504/525 nm. The ability of free AE, AE NCs, AE@RBC NCs and AE@RBC/Fe NCs to produce $^1O_2$ in the presence or absence of H_2O_2 (1 M) was measured under the same experimental conditions using the method described above. In addition, 30 μL of H_2O_2 (1 M) was added to 3 mL of different solutions containing AE NCs, AE@RBC NCs, AE@RBC/Fe NCs and ferritin, respectively, and oxygen production in the solutions was measured using a portable

dissolved oxygen meter after vigorous stirring.

2.6. In vitro cell uptake of the NCs

Cellular uptake assays were employed to verify the ability of tumor cells (HSC-3 cells) and normal cells (NIH 3T3 cells) to take up AE@RBC/Fe NCs and AE@RBC NCs. 1 mL of cells at a density of 1×10^4 cells per milliliter was seeded in a 12-well plate and incubated for 24 h before adding Cy5.5-labeled NCs at equivalent dosages and continuing the incubation for 4 h. After being washed three times with PBS, nuclei were fixed with 4% paraformaldehyde solution for 15 min and then stained with DAPI (excitation/emission wavelengths of 364/454 nm) for 10 min, followed by photographed with a confocal laser scanning microscope (CLSM; Nikon A1R, Japan). Cy5.5-labeled NCs were co-cultured with cells under the same conditions and then washed three times with PBS, followed by flow cytometry (Beckman CytoFLEX, USA) analysis of the cells after separation with trypsin. In addition, to verify that ferritin enhances the specific uptake of AE@RBC/Fe NCs by cells, cells were pretreated with excess free ferritin before the addition of AE@RBC/Fe NCs, and then examined by CLSM and flow cytometry in a similar method. Cy5.5-labeled liposomes were prepared, and AE NCs were coated with them to obtain AE@Lip NCs according to the previous report [25,26]. The macrophage line RAW264.7 was selected for testing the stealth functionality of AE@RBC/Fe NCs, AE@RBC NCs and AE@Lip NCs using a similar cell uptake assay procedure as described above.

The expression of TfR1 in HSC-3 and NIH 3T3 cells untreated with NCs was analyzed by western blot analysis. The collection of cells was made by scraping and then washed twice with ice-cold PBS. Total protein extracts prepared from RIPA lysis buffer were isolated on an SDS-PAGE according to their size and then transferred from the gel to a nitrocellulose membrane. After 1.5-h blocking with 5% nonfat milk, the overnight incubation of membranes was made with TfR1 primary antibodies at 4 °C. After rinsing with buffer, incubation with horseradish peroxidase (HRP)-conjugated secondary antibodies was continued for 1 h at room temperature, and a Gel Doc XR imaging system (Bio-Rad, Lab, Hercules, CA) was adopted to detect the signal.

2.7. Confirmation of AE@RBC/Fe NCs activated ferroptosis

2.7.1. In vitro cell viability in the presence of varied inhibitors

After culturing HSC-3 cells at a density of 5×10^3 cells per well in 96-well plates for 24 h, equal amounts of free AE, AE NCs, AE@RBC/Fe NCs (at an equivalent dosage of 10, 20, 40 μM free AE) and RBC/Fe complex (1, 2 and 4 μM) were added to each well, respectively. The culture medium was then supplemented with ferroptosis inhibitor (Fer-1, 1 μM), apoptosis inhibitor (Apo, 30 μM), and iron chelate (DFO, 100 μM) to continue the incubation for 24 h [27]. Cytotoxicity before and after the addition of inhibitors was quantified by standard MTT assay. To be brief, 20 μL of MTT (5 mg/mL in PBS) was added to each well containing the mixture and further incubated for 4 h. Afterwards, the supernatant was replaced with 150 μL of DMSO and the measurement of absorbance of the solution was made by placing it on a multimode reader at a fixed wavelength of 570 nm.

2.7.2. GSH assay

A standard GSH assay was used to detect the changes in intracellular GSH levels in the control and after different treatments. Briefly, HSC-3 cells were treated with free AE, AE NCs, AE@RBC/Fe NCs, AE@RBC/Fe NCs + Fer-1 (at an equivalent dosage of 40 μM free AE) and RBC/Fe complex (4 μM) for 24 h. Digested with trypsin, harvested cells were washed three times in PBS. The test procedure was referred to the instructions of the GSH assay kit, and the percentage content of GSH was compared with the GSH content of untreated cells.

2.7.3. Detection of LPO and mitochondrial membrane potential

Intracellular LPO levels were assessed using a BODIPY$^{581/591}$-C11 fluorescent probe according to a previously reported method [28]. HSC-3 cells were treated with different formulations as mentioned above and then washed with PBS, followed by incubation in serum-free DMEM medium with BODIPY$^{581/591}$-C11 (5 μM) for 20 min. The immediate observation and analysis of cells was made by CLSM and flow cytometry, and the excitation and emission wavelengths of green fluorescent oxidation products were 485 nm and 520 nm. The mitochondrial membrane potential of HSC-3 cells treated with different formulations was measured with the JC-1 Mitochondrial Assay Kit based on the manufacturer's guidance. Green JC-1 monomers (excitation/emission wavelengths of 488/510 nm) and red JC-1 aggregates (excitation/emission wavelengths of 561/590 nm) were observed with fluorescence microscope (Leica DMi8, Germany).

2.8. Mechanism of AE-induced ferroptosis

2.8.1. Ferroptosis-related protein expression levels

The total proteins were extracted from lysates containing cocktail protease inhibitor after treating HSC-3 cells with varied concentrations of AE NCs (0, 20, 40 and 80 μM) for 24 h and analyzed by SDS/PAGE under non-reducing conditions. Western blot analysis was performed with GPX4, JNK and GSTP1 antibody as mentioned above. Protein signals were assessed by densitometric analysis and GAPDH was used as a control.

2.8.2. Cell transfection

HSC-3 cells were stably overexpressing GSTP1 by lentiviral particles according to the manufacturer's protocol. Briefly, HSC-3 cells were cultured in DMEM medium containing 10% fetal bovine serum and replaced with fresh DMEM medium containing 10% fetal bovine serum when the cell density reached 70–80%. Then GSTP1 overexpressing lentiviral particles were added to the cell wells and continued to be cultured for 48 h. Finally, the stable cell lines that overexpress GSTP1 were selected with puromycin named GSTP1 cell group. The empty lentiviral vectors were also transfected by the same method named as Vect cell group, which was used as a negative control group for transfection. The cell transfection efficiency was detected by western blot analysis.

2.8.3. GSTP1 enzymatic activity

GSTP1 recombinant protein and intracellular GSTP1 activity were measured using a fluorescence-based GST activity kit according to the manufacturer's protocol. GSTP1 activity is defined as the amount of enzyme for catalyzing the reaction of GSH and monochlorobiphenyl, which in its free form is barely fluorescent and fluoresces blue upon reaction with GSH catalyzed by GST. Briefly, after treating GSTP1 and Vect cell with 40 μM of AE NCs for 24 h, homogenization and centrifugation were adopted to collect the supernatant. The untreated cells were adopted as control. The samples and standards were placed in a 96-well plate with excitation wavelength fixed at 380 nm, and the fluorescence change at 461 nm was collected to determine GSTP1 activity. In addition, different concentrations of AE NCs were reacted with GSTP1 recombinant protein for 24 h and then the enzymatic activity was determined using the same method.

2.8.4. AE induces ferroptosis in GSPT1 overexpression cells

The GSTP1 and Vect cell were treated with the same concentration of AE NCs (40 μM), and untreated cells were adopted as control. The cell viability, LPO and mitochondrial membrane potential were measured according to the mentioned method.

2.9. Measurement of intracellular oxygen content

After inoculation in 96-well plates at a density of 6×10^3 cells per well, HSC-3 cells were cultured for 24 h. Subsequently, cells were treated with free AE, AE NCs, and AE@RBC/Fe NCs for 4 h at the same

AE dose. Cells treated with PBS were used as controls. Fluorescence intensity at 650 nm was measured using the Extracellular Oxygen Consumption Assay Kit (Abcam, ab197243), and changes in cellular oxygen content were analyzed based on the manufacturer's protocol.

2.10. Detection of intracellular ROS

Fluorescence microscope and flow cytometry were adopted to detect intracellular ROS production referring to the previously reported literature [29]. Briefly, the 24 h culture of HSC-3 cells was made in 24-well plates, followed by the addition of free AE, AE NCs, and AE@RBC/Fe NCs at the AE dose of 40 μM to treat the cells for 4 h. Replaced with serum-free medium containing DCFH-DA, the cell was further incubated for 15 min at 37 °C in the dark. Afterwards, parallel cell groups were irradiated with laser at 405 nm for 5 min and washed carefully twice with PBS. Fluorescence images of the cells were captured with fluorescence microscope, corresponding to excitation and emission wavelengths of 488 and 515 nm. Flow cytometry determination of ROS levels was similar to the cell treatment method mentioned above, except that the fluorescence signal was analyzed by digesting the cells and collecting them in a flow tube.

2.11. In vitro cytotoxicity and apoptosis

HSC-3 cells were cultured in 96-well plates at a density of 6×10^3 cells per well for 24 h, and then 100 μL of free AE, AE NCs and AE@RBC/Fe NCs with gradient concentrations of free AE were added to each well for 24 h. After that, the cells were irradiated with 405 nm laser for 5 min and then continued to be cultured for 24 h. The viability of cells *in vitro* with or without laser radiation was analyzed by the MTT method mentioned above. To visualize the inhibitory effect of various formulations on HSC-3 cells, the cells were treated identically followed by staining with Calcein-AM and PI for 20 min on viable and dead cells. The cells were subsequently washed carefully with PBS and the cell images were observed by fluorescence microscope. For apoptosis analysis against treated HSC-3 cells, cells were collected by trypsin digestion and stained with annexin V-FITC and PI and then analyzed by flow cytometry.

2.12. Morphological changes of ferroptosis and apoptosis

The morphological variations of the cells were observed by bio-TEM (JEM-1400, JEOL, Japan) considering the AE@RBC/Fe NCs induced ferroptosis and PDT effects. Briefly, HSC-3 cells and AE@RBC/Fe NCs were co-cultured for 24 h after irradiation to 405 nm of laser for 5 min. The cells were fixed with electron microscope fixative before and after laser irradiation at 4 °C. Untreated cells were employed as controls. The dehydration of cells was made in graded ethanol at 70, 90, 96 and 100%, followed by embedding in EPON 812 epoxy resin, sectioning, positive staining with uranium and lead salts for bio-TEM imaging to observe cellular ultrastructural changes.

2.13. Pharmacokinetic evaluation

All animal experimental protocols were approved by the Animal Care and Use Committee of Chengdu medical college and were conducted in strict accordance with the Institutional Health Guide for the Care and Use of Laboratory Animals of China. Briefly, Sprague Dawley rats were injected with free AE, AE NCs and AE@RBC/Fe NCs (RBC membrane fragments from Sprague Dawley rats) at an equal AE dose of 7.5 mg/kg through the tail vein. The collection of blood samples (0.5 mL) was made from the orbital venous plexus at presented time points and plasma was collected by centrifugation. AE concentrations in plasma were measured by fluorescence spectrophotometer and pharmacokinetic parameters were calculated using PKsolver.

2.14. In vivo distribution of AE@RBC/Fe NCs

HSC-3 Xenografted tumor model was established by subcutaneously injecting HSC-3 tumor cells (2×10^6 cells) into the right inguinal location of Balb/c nude mice (4 weeks old, 15–18 g). When the tumor volume reached approximately 100 mm^3, mice were used for distribution studies of AE@RBC/Fe NCs *in vivo*. Mice were randomly assigned into two groups ($n = 3$) and received injection with free AE and AE@RBC/Fe NCs by the tail vein at an equivalent AE dose of 7.5 mg/kg, respectively. The tumors and major organs (*e.g.*, heart, liver, spleen, lung, kidney) were harvested from sacrificed mice after 1 and 24 h of administration. The collected tissues were repeatedly rinsed with PBS to remove blood and the tissues were homogenized to extract AE from the supernatant, followed by determination of AE content by the method mentioned above. The level of distribution in the tissue was defined as the proportion of the actual quantity of drug in the tissue to the total quantity of injected drug and normalized to the tissue weight (% ID/g). In addition, mice were photographed at excitation/emission wavelengths of 670/700 nm by tail vein injection of identical doses of Cy5.5-labeled AE@RBC NCs and AE@RBC/Fe NCs at some specific time points applying an IVIS imaging system (Caliper Life Sciences Inc., USA) to record fluorescence changes in mice. Some mice were euthanized after 24 h of administration, and major organs and tumors were collected for the fluorescence distribution analysis *ex vivo* as mentioned above.

2.15. In vivo antitumor mechanisms of AE@RBC/Fe NCs

Mice bearing HSC-3 tumors were randomly assigned into three groups ($n = 3$) for exploring the mechanism of combination therapy. When the tumor reached approximately 100 mm^3, tail-vein injection with saline, AE@RBC/Fe NCs and AE@RBC/Fe NCs + laser was executed separately to the three groups (equivalent AE dose of 7.5 mg/kg). After 24 h, one group of mice treated with AE@RBC/Fe NCs were irradiated to 405 nm laser for 5 min. Mice were euthanized at the designated times, tumor tissues were collected to measure JNK and p-JNK change using western blot assay. To examine the GSH levels and GSTP1 activity of the tumors, the harvested tumors from the mice were assayed according to the protocol of the kit. Malondialdehyde (MDA) content was measured in tumor tissue with a TBARS assay kit to monitor lipid peroxidation according to the manufacturer's instructions. Immunohistochemical (IHC) staining of 4-HNE was performed using an anti-4-HNE monoclonal antibody according to the manufacturer's instructions for assessment of lipid peroxidation. The tumor tissues were fixed with 3% glutaraldehyde and 1% OsO_4 successively. Then the samples were dehydrated and embedded. Ultrathin sections were stained and observed with bio-TEM.

2.16. In vivo antitumor evaluation

Mice bearing HSC-3 tumors were fallen into five groups (saline, free AE, AE NCs, AE@RBC/Fe NCs and AE@RBC/Fe NCs + laser) randomly, and each group consisting of 9 mice. When the tumor volume reached approximately 100 mm^3, mice in each group received intravenous injection with 100 μL of corresponding formulation at a relative AE dose of 7.5 mg/kg per mouse. After 24 h, the mice treated with AE@RBC/Fe NCs were irradiated to 405 nm laser for 5 min. Measured every two days starting from the first day after laser irradiation, the calculation of tumor size was made by the formula $V = (L \times W^2)/2$, where L and W represent the longest and shortest diameter of the tumor. The number of live animals at every time point was recorded to plot into Kaplan-Meier survival curves and analyzed to obtain the median survival time. On day 21 after treatment, tumors from partially sacrificed animals ($n = 3$) were collected and histologically examined based on a standard hematoxylin and eosin (H&E) staining protocol. In addition, tumor cell proliferation and apoptosis were analyzed by performing IHC assessment of Ki-67 and caspase-3 on tumor sections. The positively stained cells were counted

under a light microscope and the total number of cells in these regions was normalized.

2.17. Biosafety of AE@RBC/Fe NCs

The treatment safety of AE@RBC/Fe NCs was evaluated by body weight change, biochemical analysis and histological examination of major organs. The body weights of mice treated with different formulations were measured every two days. At the end of the indicated treatment, the major organs (heart, lung, spleen, liver, and kidney) of the sacrificed mice were harvested and stained with H&E staining protocols for histological examination. Healthy BALB/c mice (n = 3) received intravenous injection with PBS and AE@RBC/Fe NCs (7.5 mg/kg), and blood was collected after 3 days for analysis of blood markers (red blood cells, RBC; hemoglobin, HGB; white blood cells, WBC; platelets, PLT), hepatotoxicity (alanine aminotransferase, ALT; aspartate aminotransferase, AST; alkaline phosphatase, ALP), cardiotoxicity (creatine kinase, CK) and nephrotoxicity (blood urea nitrogen, BUN) by Blood Biochemistry Analyzer (MNCHIP POINTCARE) and Auto Hematology Analyzer (MC-6200VET) [30].

2.18. Statistical analysis

In this work, mean standard deviation (SD) is used for the reported results. Whenever appropriate, multiple groups were compared by analysis of variance (ANOVA), and the statistical difference between the two groups was revealed by a two-tailed Student's *t-test*. A probability value (p) of smaller than 0.05 was considered statistically significant.

3. Results and discussion

3.1. Physicochemical characterizations of AE@RBC/Fe NCs

In this study, AE NCs were prepared in one step by a facile emulsification method and used as a core to decorate the surface with RBC membranes and ferritin. TEM images show the typical sphere-like structure of the naked AE NCs with a high AE encapsulation efficiency of 92.6% (Fig. 1a). AE NCs were formed at a ratio of 1:5 of AE to P407, resulting in a maximum drug-loading ratio of up to 16.7%. The AE@RBC/Fe NCs exhibited a distinct core-shell structure with an external lipid bilayer shell, and their particle size exhibits a slight increase (112 ± 3 nm) compared to AE NCs (100 ± 2 nm) (Fig. 1b), indicating that the RBC membranes was successfully wrapped around the AE NCs. To enhance the target activity of biomimetic AE NCs to tumor cells, ferritin was modified as a recognition component together with RBC membranes on the surface of AE NCs by multiple co-extrusion through porous membranes. As shown in Fig. 1c, the energy-dispersive spectroscopy (EDS) elemental mapping analysis pointed to the presence of Fe and P elements in AE@RBC/Fe NCs, which clearly indicating that the cell membrane interspersed with ferritin was successfully coated on the surface of the AE NCs. The iron content in AE@RBC/Fe NCs was further determined to be 0.27 wt% by ICP-OES analysis. In addition, the protein ingredients of AE@RBC/Fe NCs were further analyzed by SDS-PAGE and the bands corresponding to membrane proteins and ferritin

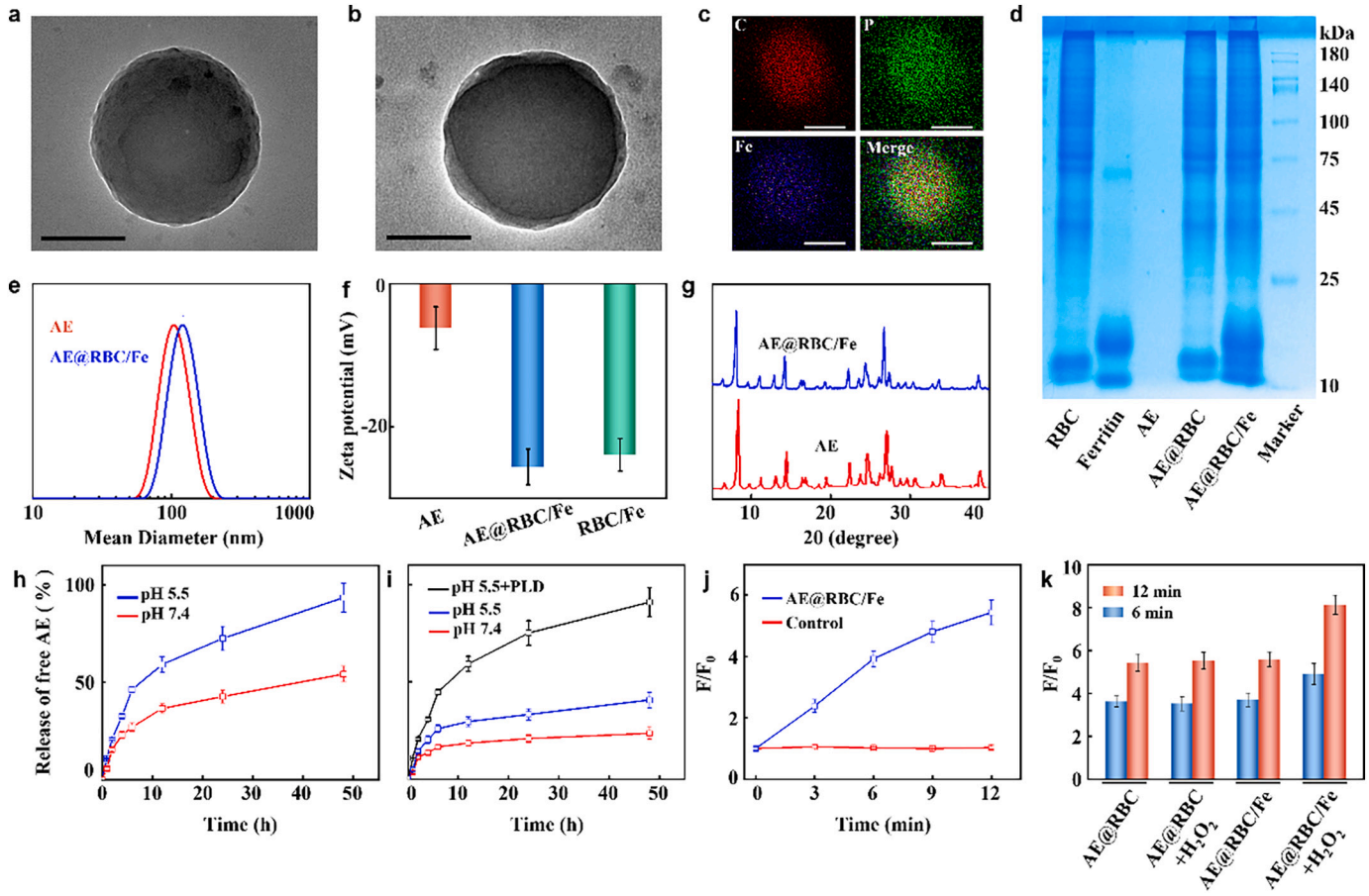

Fig. 1. Characterization of AE@RBC/Fe NCs. TEM images of (a) AE NCs and (b) AE@RBC/Fe NCs (Scale bar: 50 nm). (c) Elemental mapping of AE@RBC/Fe NCs (Scale bar: 50 nm). (d) SDS-PAGE protein analysis of RBC, ferritin, AE NCs, AE@RBC NCs and AE@RBC/Fe NCs. (e) Hydrodynamic size and (f) zeta potential (n = 3) and (g) PXRD patterns of NCs. *In vitro* release profiles of free AE from (h) AE NCs and (i) AE@RBC/Fe NCs after incubation in different conditions (n = 3). (j) *In vitro* $^1O_2$ generation of AE@RBC/Fe NCs under 405 nm laser irradiation for a continuous time (n = 3). (k) *In vitro* $^1O_2$ generation of AE@RBC NCs and AE@RBC/Fe NCs with or without H_2O_2 under 405 nm laser irradiation (n = 3).

were observed in the protein profile of AE@RBC/Fe NCs (Fig. 1d), indicating that membrane proteins and ferritin were completely retained during the fusion process of AE@RBC/Fe NCs. The membrane protein content of AE@RBC/Fe NCs was rightfully increased compared to naked AE NCs and was further quantified as 80.3 ± 5.1 μg/mg using the protein standard curve (Fig. S1). DLS data in Fig. 1e exhibited that the average hydrodynamic diameter of AE@RBC/Fe NCs increased slightly from 106 ± 5 to 120 ± 10 nm after cell membrane and protein coating, and both were well dispersed in PBS buffer in any case. In addition, the zeta potential of AE@RBC/Fe NCs turned out to be close to the zeta potential of the RBC/Fe complex (−23.9 ± 2.3 mV) at −25.6 ± 2.5 mV, demonstrating the coating RBC membrane was present in the right-side-out orientation (Fig. 1f) [31]. Moreover, the orientation of RBC membrane on the AE@RBC/Fe NCs surface could be assessed by quantification of glycoprotein, which exclusively distributed on the extracellular side of membranes [22]. As shown in Fig. S2a, the average content of glycoprotein detached from AE@RBC/Fe NCs is around 91.1% of the equivalent amount in free RBC vesicles. This quantification indicated that the majority of the glycoproteins were present on the outside surface of the AE@RBC/Fe NCs, further confirming the "right-side-out" orientation of the RBC membrane on the NCs. RBC membranes and negatively charged nanoparticle cores have been shown to be favorable for the formation of a full cell membrane coating [23]. In order to probe the integrity of the cell membrane coating, the bare core AE NCs needed to be replaced by the fluorescent NBD-labeled AE NCs prior to cell membrane coating. AE@RBC NCs and AE@RBC/Fe NCs were treated with DT, a negatively charged reducing agent that cannot cross the membrane [32]. DT reduced NBD to 7-amino-2,1,3-benzoxadiazole (ABD), which irreversibly quenched the fluorescence of the exposed NBD-labeled NCs. The ratio of full coating of AE@RBC NCs and AE@RBC/Fe NCs was calculated as 10.16% and 9.45% by comparing the reserved fluorescence intensity with the initial fluorescence intensity before DT addition, indicating that the co-extrusion process is an efficient method in the formation of a full cell membrane coating (Fig. S2b). The PXRD patterns of AE NCs and AE@RBC/Fe NCs were depicted in Fig. 1g. There was no significant difference between the two PXRD patterns, indicating that AE NCs maintained the same crystal structure and crystallinity before and after coated with the cell membrane and ferritin. Of note, AE@RBC/Fe NCs showed an almost constant hydrodynamic size distribution (Fig. S3a), polydispersity index (Fig. S3b) and surface protein content (Fig. S3c) in PBS over 7 days, demonstrating its excellent stability, which is crucial for subsequent *in vivo* applications.

3.2. Verification of the drug release and $^1O_2$ generating ability

The purpose of the cell membrane coating is to maintain the stability of AE@RBC/Fe NCs in the systemic circulation while can be disassembled to release the drug through PLD-catalyzed phospholipid hydrolysis in cancer cells [33]. Based on this belief, we studied the release rate of AE in mimetic normal microenvironment (pH 7.4) and tumor microenvironment containing PLD (pH 5.5). As shown in Fig. 1h, the acidic solution (pH 5.5) prompted an abrupt release of AE from AE NCs in the initial phase, in marked contrast to the release level from the neutral solution (pH 7.4), which was associated with better solubility of AE in the acidic environment [34]. In contrast, AE@RBC/Fe NCs showed a relatively flat release profile in PBS buffer of either pH 7.4 or pH 5.5, with only 23.6% and 40.7% of AE released within 48 h, confirming the protective effect of cell membrane coating for AE NCs. This feature allowed AE@RBC/Fe NCs rapid accumulating in the tumor site with delayed dissolution rate of the drug in the blood, and achieved the minimum drug concentration for therapeutic effect. Unsurprisingly, a burst release of AE was observed in PBS buffer (pH 5.5) containing PLD, with a release of up to 90.9% during 48 h (Fig. 1i). Meanwhile, similar morphological changes based on PLD-dependent degradation were observed in the TEM images of AE@RBC/Fe NCs. Fig. S4 showed that the naked AE NCs have almost no intact structure under acidic conditions for the rapid hydrolysis of the outer phospholipid protective membrane of AE@RBC/Fe NCs by PLD, and only the irregular shapes forming from the aggregation of redispersed AE nanoparticles can be observed. However, in the absence of PLD, the morphology of AE@RBC/Fe NCs retained their original shape in PBS buffer (pH 7.4) for 6 h. These results suggest that AE@RBC/Fe NCs can rapidly release drugs in response to tumor cell environment where PLD is over-expressed.

Previous reports have confirmed that ferritin can release Fe^{3+} under acidic conditions [15], which can be reduced to Fe^{2+} by GSH, further triggering the Fenton reaction to convert H_2O_2 to •OH. As shown in Fig. S5a, the Fe^{2+} indicator *o*-phenanthroline appeared pale yellow after dispersion of AE@RBC/Fe NCs in acidic solution for 4 h, consistent with the indicator in the Fe^{3+} control solution. However, when GSH was added, the color of the indicator solution changed rapidly due to the formation of an orange complex as a result of the specific reaction between *o*-phenanthroline and Fe^{2+}, a reduzate deriving from the reduction of Fe^{3+} by GSH. In addition, the reintroduction of H_2O_2 caused the oxidation of Fe^{2+} to Fe^{3+}, accompanied by a rapid recovery of the color of the solution. The *o*-phenanthroline absorption of corresponding groups at 512 nm was shown in Fig. S5b. These observations suggest that Fe^{3+} released from AE@RBC/Fe NCs enables iron cycling through GSH and H_2O_2 (Fig. S5c).

$^1O_2$ is one of the essential elements of PDT and its production is directly related to the effectiveness of PDT treatment [35]. In this study, SOSG was used as a probe to monitor $^1O_2$ production by AE@RBC/Fe NCs in PLD-containing PBS buffer (pH 5.5). As shown in Fig. 1j, the fluorescence intensity of SOSG incubated with AE@RBC/Fe NCs gradually increased as the radiation time from 0 to 12 min, but there was no significant change in SOSG alone, indicating the excellent $^1O_2$ production capacity of AE@RBC/Fe NCs under irradiation. Notably, the $^1O_2$ production of AE NCs was decreased compared to that of the free AE solution, which may be related to the aggregation-caused quenching (Fig. S6) [36]. In addition, we further investigated the effect of ferritin and H_2O_2 on the $^1O_2$ content produced by AE@RBC/Fe NCs. As shown in Fig. 1k, the fluorescence intensity of SOSG was similar after the addition of AE@RBC NCs and AE@RBC/Fe NCs. However, the SOSG fluorescence intensity of the AE@RBC NCs and AE@RBC/Fe NCs groups showed a significant difference after the addition of H_2O_2. The fluorescence intensity of the "AE@RBC/Fe NCs + H_2O_2" group increased drastically with the extension of laser radiation time, indicating that H_2O_2 could promote AE@RBC/Fe NCs photoactivation to produce more sufficient $^1O_2$. Interestingly, the addition of H_2O_2 did not interfere at all with the fluorescence intensity of SOSG in the AE@RBC NCs group, demonstrating that only the simultaneous presence of ferritin and H_2O_2 could enhance the efficiency of $^1O_2$ production. Yu et al. constructed a nanoparticle with self-improved PDT efficacy through the self-assembly of chlorin e6 (Ce6) and hemin, which overcame the therapeutic defects of conventional PDT in tumor hypoxic environment, mainly because Fe-containing hemin could catalyze endogenous H_2O_2 to produce sufficient oxygen and then be converted into more cytotoxic $^1O_2$ by the Ce6 [37]. Given this type of Fe-containing protein can catalyze the production of oxygen from H_2O_2 *via* the Fenton reaction, we analyzed that AE@RBC/Fe NCs can induce high-level $^1O_2$ in the presence of H_2O_2 for that the oxygen can be produced from H_2O_2 through Fe-catalyzed Fenton reaction, which can be further converted to $^1O_2$ by AE. To this end, we verified the hypothesis that AE@RBC/Fe NCs can generate oxygen by dissolved oxygen experiments, and only ferritin and AE@RBC/Fe NCs could induce the oxygen production from H_2O_2 under acidic conditions containing PLD compared with other controls (Fig. S7).

3.3. Cellular uptake study of AE@RBC/Fe NCs

RBC membranes was supposed to be adept in immune tolerance due to the presence of immunomodulatory markers (*e.g.* CD47) [38], we wondered whether AE@RBC/Fe NCs could inherit stealth properties from their RBC membrane-derived coating. To answer this question, we

first investigated the cellular uptake behavior of RAW 264.7 macrophages against AE@RBC/Fe NCs. As showed in Fig. S8, AE@RBC/Fe NCs and AE@RBC NCs exhibit much lower uptake profile by RAW264.7 compared to AE@Lip NCs from CLSM and flow cytometry. This prominent reduce of uptake by macrophage cells confirmed that biomimetic camouflage through RBC membranes can confer the potential for AE@RBC/Fe NCs to effectively evade immune recognition [39].

Effective uptake of the nanoscopic dosage forms by cancer cells is critical for superior anticancer efficacy. Therefore, the internalization of AE@RBC/Fe NCs labeled with Cy5.5 was investigated by CLSM and flow cytometry. As shown in Fig. 2a, the red fluorescence presented in AE@RBC/Fe NCs-treated HSC-3 cells was significantly stronger than

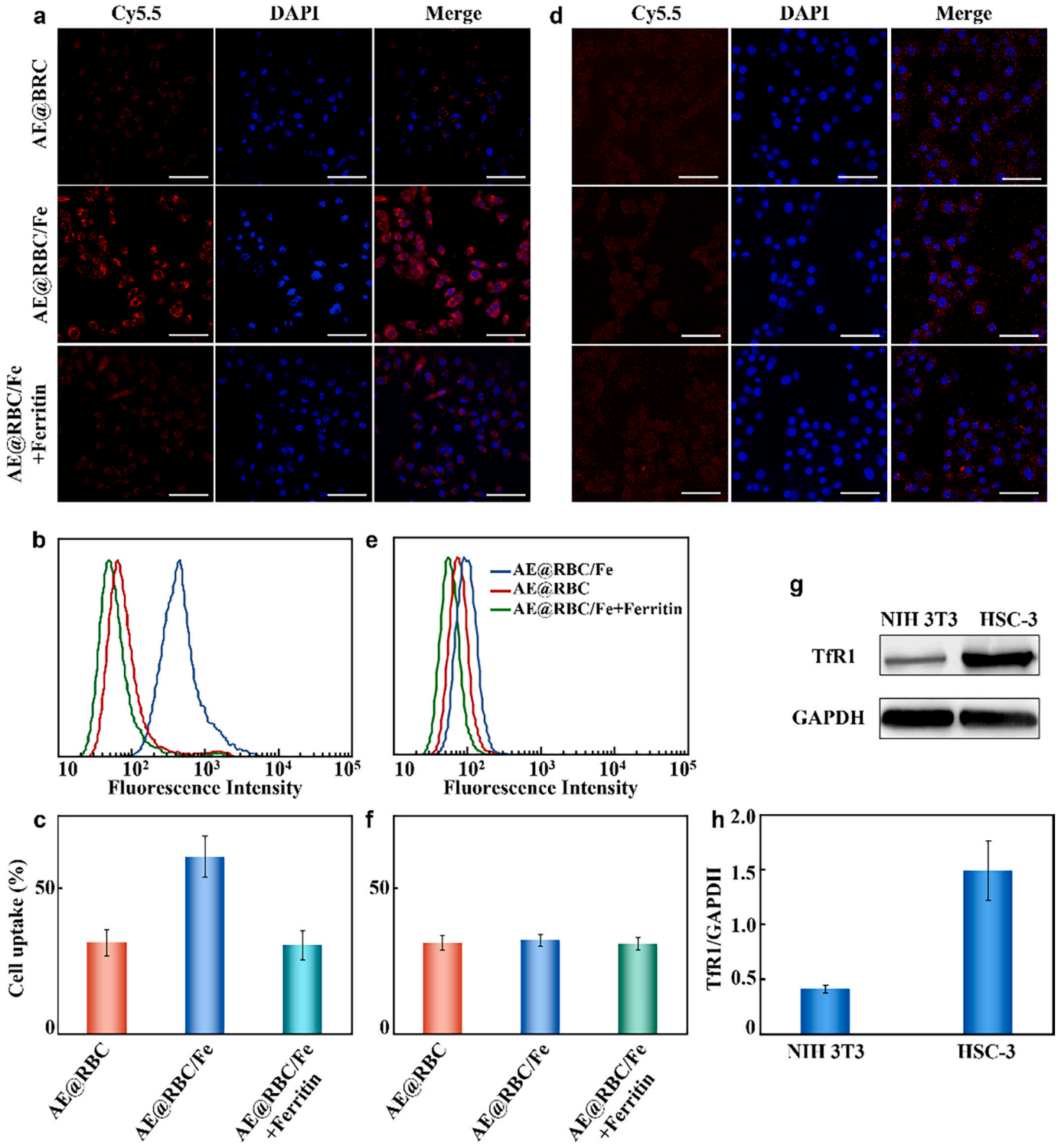

Fig. 2. Cellular uptake of AE@RBC NCs and AE@RBC/Fe NCs. (a) CLSM images (Scale bar: 50 μm) and (b) flow cytometry analysis and (c) cellular uptake amount (n = 5) of HSC-3 cells after the treatment with Cy5.5 labeled AE@RBC NCs and AE@RBC/Fe NCs. (d) CLSM images (Scale bar: 50 μm) and (e) flow cytometry analysis and (f) cellular uptake amount (n = 5) of NIH 3T3 cells after the treatment with Cy5.5 labeled AE@RBC NCs and AE@RBC/Fe NCs. (g) Western blot and (h) quantitative analysis (n = 3) of TfR1 expression in HSC-3 and NIH 3T3 cells.

that of cells treated with AE@RBC NCs, and the quantitative results of flow cytometry demonstrated this excellent result (Fig. 2b). It can be seen from Fig. 2c that the uptake efficiency of AE@RBC/Fe NCs in HSC-3 cells within 4 h was more than 60.9%, which was 1.9 times higher than that of AE@RBC NCs. However, the internalization differences of AE@RBC/Fe NCs and AE@RBC NCs were not reflected in the control cells (NIH 3T3 cells), the results of both CLSM images (Fig. 2d) and quantitative flow cytometry analysis (Fig. 2e) indicated that NIH 3T3 cells exhibited similar uptake efficiency for the two types of NCs (Fig. 2f). Collectively, the red fluorescence of HSC-3 cells after AE@RBC/Fe NCs treatment was more prominent compared to NIH 3T3 cells, reflecting the highly specific targeting ability of AE@RBC/Fe NCs to HSC-3 cells. To verify that this targeting ability is based on the specific binding between the ferritin on the surface of AE@RBC/Fe NCs and membrane protein TfR1, we explored the expression difference of TfR1 in HSC-3 and NIH 3T3 cells by western blot analysis. Fig. 2g and h showed that TfR1 was highly expressed in HSC-3 cells compared to NIH 3T3 cells, thus the uptake efficiency of AE@RBC/Fe NCs in HSC-3 over 4 h was 2 times higher than that of control cells (NIH 3T3). Furthermore, the internalization of AE@RBC/Fe NCs was significantly inhibited when cells were treated with excess free ferritin in advance, in response to competitive inhibition or surface receptor blockade (Fig. 2a-c). All these results suggest that ferritin-modified AE@RBC/Fe NCs possesses high targeting affinity for cancer cells with over-expressed TfR1.

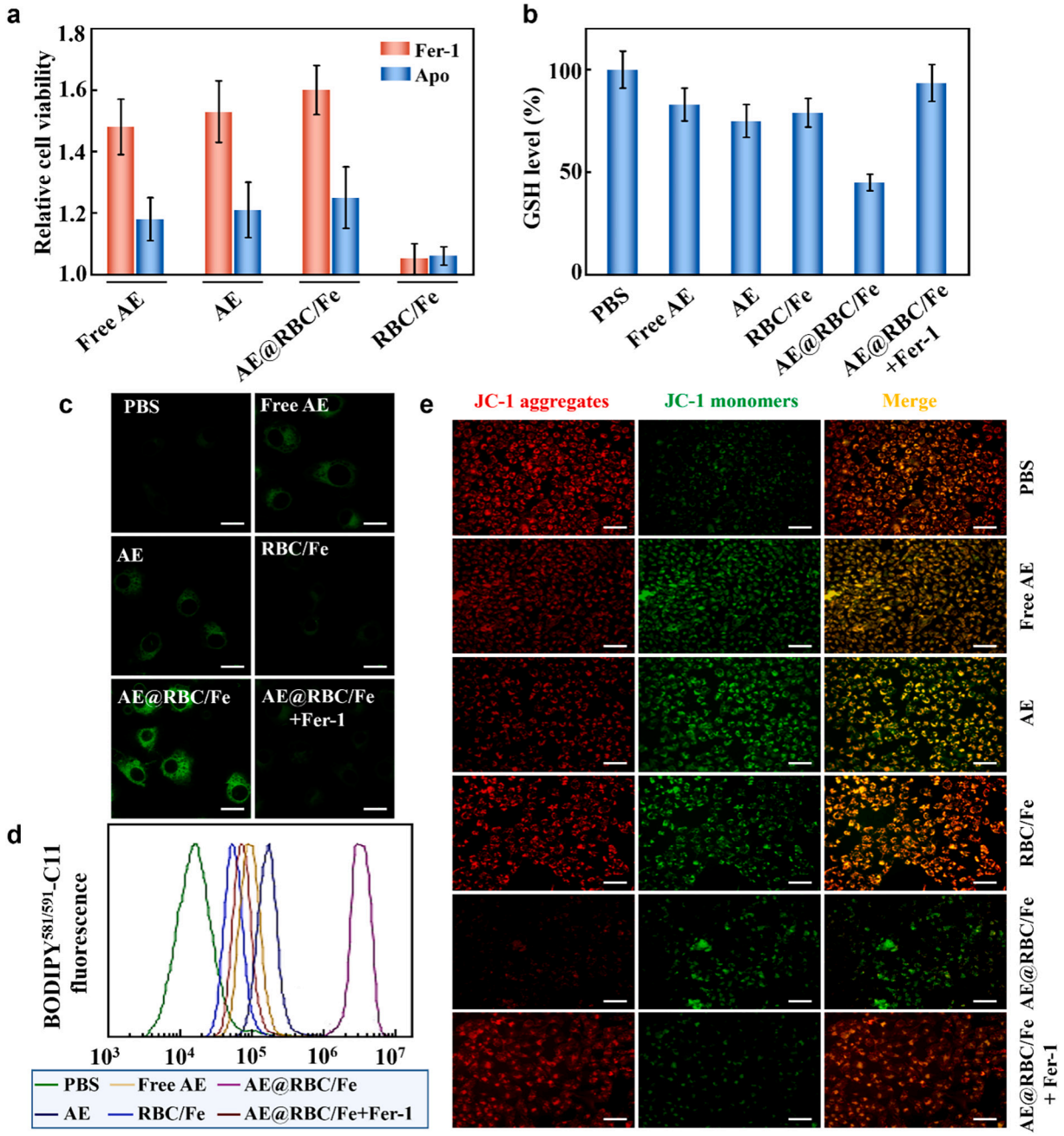

Fig. 3. Confirmation of AE@RBC/Fe NCs-mediated ferroptosis in HSC-3 cells. (a) Relative cell viability of HSC-3 cells treated with free AE, AE NCs, AE@RBC/Fe NCs (at an equivalent dosage of 40 μM free AE) and RBC/Fe complex (4 μM) after the addition of Fer-1 (1 μM) and Apo (30 μM), respectively ($n = 3$). (b) Intracellular GSH level of HSC-3 cells after different treatments ($n = 3$). (c) CLSM images (Scale bar: 10 μm) and (d) flow cytometry assay of cellular LPO by BODIPY$^{581/591}$-C11 staining after the treatment with different formulations. (e) Mitochondria membrane potential analysis by JC-1 staining after the treatment with different formulations (Scale bar: 50 μm).

3.4. Ability of AE@RBC/Fe NCs inducing ferroptosis

For clarifying the death mode induced by AE@RBC/Fe NCs, HSC-3 cells were treated with Fer-1 (ferroptosis inhibitor) or Apo (apoptosis inhibitor), respectively, prior to the cytotoxicity assay [27]. To eliminate the possible effects of PDT, laser irradiation was not used in this session to allow independent investigation of the anti-tumor pathway of AE@RBC/Fe NCs. As shown in Fig. 3a, the cytotoxicity of cells treated with free AE, AE NCs and AE@RBC/Fe NCs in the presence of Fer-1 or Apo was alleviated to varying degrees, and the Fer-1-induced rescue was more pronounced than that induced by the addition of Apo. In contrast, the addition of Fer-1 and Apo showed negligible cytotoxic effects on RBC/Fe complex treated cells. These results suggest that the AE-induced cell death pathway may involve both ferroptosis and apoptosis, and that the ferroptosis dominates relative to apoptosis. AE-induced apoptosis has been clearly confirmed by previous studies [40–42], however, there is no relevant research on AE-induced ferroptosis so far. Fer-1 still exhibited a stronger mitigating effect on cytotoxicity at different AE concentrations (Fig. S9), and notably this mitigating effect increased with increasing AE concentration, suggesting that the ferroptosis appears to be more profound at higher AE concentrations. The reduction of GSH levels is often considered as a symbolic event in the ferroptosis process for that the cytotoxic •OH produced in ferroptosis can oxidize intracellular GSH [43]. As can be seen from Fig. 3b, HSC-3 cells treated with free AE (83%), AE NCs (75%) and RBC/Fe (79%) showed relatively lower intracellular GSH levels compared to the PBS-treated control group (~100%). The trend toward reduced GSH levels was even more pronounced in AE@RBC/Fe NCs-treated cells, with the relative reduction exceeding the sum of the AE NCs and RBC/Fe-treated cells alone. However, the GSH levels increased sharply when Fer-1 was added beforehand, almost as much as in the control group. These findings clearly indicate that GSH depletion is indeed attributable to ferroptosis, and that AE@RBC/Fe NCs provides a stronger destruction of intracellular antioxidative defense system of cancer cells compared to naked AE NCs.

The production of large amounts of LPO in cells is an important biomarker of ferroptosis and a key determinant of its lethality [44]. As a lipid peroxidation sensor, BODIPY$^{581/591}$-C11 was used to study the production of LPO by CLSM. Fig. 3c showed that HSC-3 cells treated with free AE, AE NCs and AE@RBC/Fe NCs displayed distinct green fluorescence on the cell membrane compared to PBS-treated controls, indicating the production of LPO in the cells. However, the fluorescence intensity of AE@RBC/Fe NCs-treated cells was significantly reduced when Fer-1 was added simultaneously. The change in LPO production again confirmed that AE-induced cytotoxicity is inextricably linked to ferroptosis. Quantitative analysis by flow cytometry was consistent with the observations of CLSM and clearly showed that AE@RBC/Fe NCs-treated HSC-3 cells produced more LPO (stronger green fluorescence on the cell membrane) than free AE or AE NCs treatment, implying that Fe^{3+} provided by ferritin can promote the ferroptosis process (Fig. 3d). In addition, abnormal alterations in membrane potential due to mitochondrial damage are an important early warning of ferroptosis. We assessed mitochondrial function with a membrane-permeable JC-1 dye, which accumulating in the healthy mitochondrial matrix to form red fluorescent JC-1 aggregates (high mitochondrial membrane potential), but causing a shift in fluorescence to green JC-1 monomers (low mitochondrial membrane potential) with the occurrence of mitochondrial dysfunction [45]. As shown in Fig. 3e, the decrease in red fluorescence was accompanied by an increase in green fluorescence in cells treated with free AE, AE NCs and AE@RBC/Fe NCs, whereas the PBS control was predominantly red fluorescence. Further study revealed that the addition of Fer-1 reduced the mitochondrial depolarization treated by AE@RBC/Fe NCs and maintained the high membrane potential of mitochondria. This result is consistent with the production of LPO, that because an abnormal change in membrane potential reflected an increase in mitochondrial electron transport chain activity, which contributing to LPO accumulation [46]. We logically validated the role of Fe^{3+} in AE@RBC/Fe NCs-treated cells considering that ferroptosis is an iron-dependent mode of programmed cell death. In comparison with other groups, DFO, an iron chelator, was shown to significantly suppress the sensitivity of cells to AE@RBC/Fe NCs-induced damage. Both cell viability and GSH levels recovered following DFO addition, suggesting that iron is essential in this treatment (Fig. S10). Together, these valuable results suggest that AE@RBC/Fe NCs-induced cytotoxicity is closely related to ferroptosis mediated by AE, and definitively indicate that Fe^{3+} supplied from ferritin makes a significant contribution to enhance the effect of ferroptosis.

3.5. Mechanism of AE-induced ferroptosis

To investigate the mechanisms of AE-induced ferroptosis, we first verified the effect of AE on the expression of lipid repair enzyme GPX4, a key protein that directly or indirectly inducing ferroptosis, and its abnormal expression impairs cellular antioxidant defense [47]. However, the results of western blot analysis revealed that the expression of GPX4 was not downregulated in HSC-3 cells after treated with AE NCs of different concentrations (Fig. S11). This unexpected result suggests that there may be other key substrates that trigger ferroptosis. As an important stress response mitogen activated protein kinase, JNK was significantly and consistently activated when cells were treated with AE, thereby inducing apoptosis [12]. In the meantime, previous literature has confirmed that the binding of GSTP1 to JNK inhibits the phosphorylation/activation of JNK (Fig. 4a) [48]. The two opposing effects on JNK logically prompted us to explore whether AE exerts a regulatory effect on GSTP1. As shown in Fig. 4b and Fig. S12, AE NCs treatment induced substrate phosphorylation/activation of JNK on the basis of unchanged total JNK, but insignificant abnormal expression of GSTP1. To further investigate the effect of AE NCs on GSTP1 activity, the change of GSTP1 in activity was measured by the reaction between AE NCs with different concentrations and GSTP1 recombinant protein, and the results showed that the activity of GSTP1 diminished with the increasement of AE NCs (Fig. 4c). These results suggest that AE may be a potential inhibitor of GSTP1 although it does not interfere with the expression of GSPT1.

Inspired by the inhibition of GSPT1 recombinant protein activity by AE NCs, the inhibitory effect of AE NCs on intracellular GSTP1 was further clarified by transfection of HSC-3 cells with GSPT1 overexpression lentiviral particles. Significantly increased protein levels in the GSTP1 group were found compared to the Vect group transfected with empty vector (Fig. S13). HSC-3 cells from both groups were subsequently treated with AE NCs (40 μM) and tested for intracellular GSTP1 activity, the results in Fig. 4d showed that the relative activity of GSTP1 was reduced compared to the control group regardless of whether GSTP1 protein expression was increased.

This positive finding tentatively establishes that AE-induced ferroptosis may be caused by inhibiting the activity of intracellular GSTP1. This also plausibly explains that AE causes redox imbalance and depletes intracellular GSH, which binds to GSTP1 and detoxifies electrophiles in the physiological state [49]. Next, we treated GSTP1 group and Vect group with the equivalent concentration of AE NCs (40 μM) and found significant changes in cell viability (Fig. 4e), LPO levels (Fig. 4f) and mitochondrial membrane potential (Fig. 4g), all of which are significant features of ferroptosis. It is of interest to note that the overexpression of GSTP1 alleviated the ferroptosis process to some extent compared to Vect groups, which strongly confirming that AE induces the onset of ferroptosis by inhibiting GSTP1 activity.

3.6. In vitro anticancer effects of AE@RBC/Fe NCs

The release of Fe^{3+} from AE@RBC/Fe NCs to supply cancer cells with sufficient oxygen based on the Fenton reaction is essential to achieve synergistic treatment of ferroptosis and PDT. To this end, we measured the dissolved oxygen in the culture medium of HSC-3 cells using an

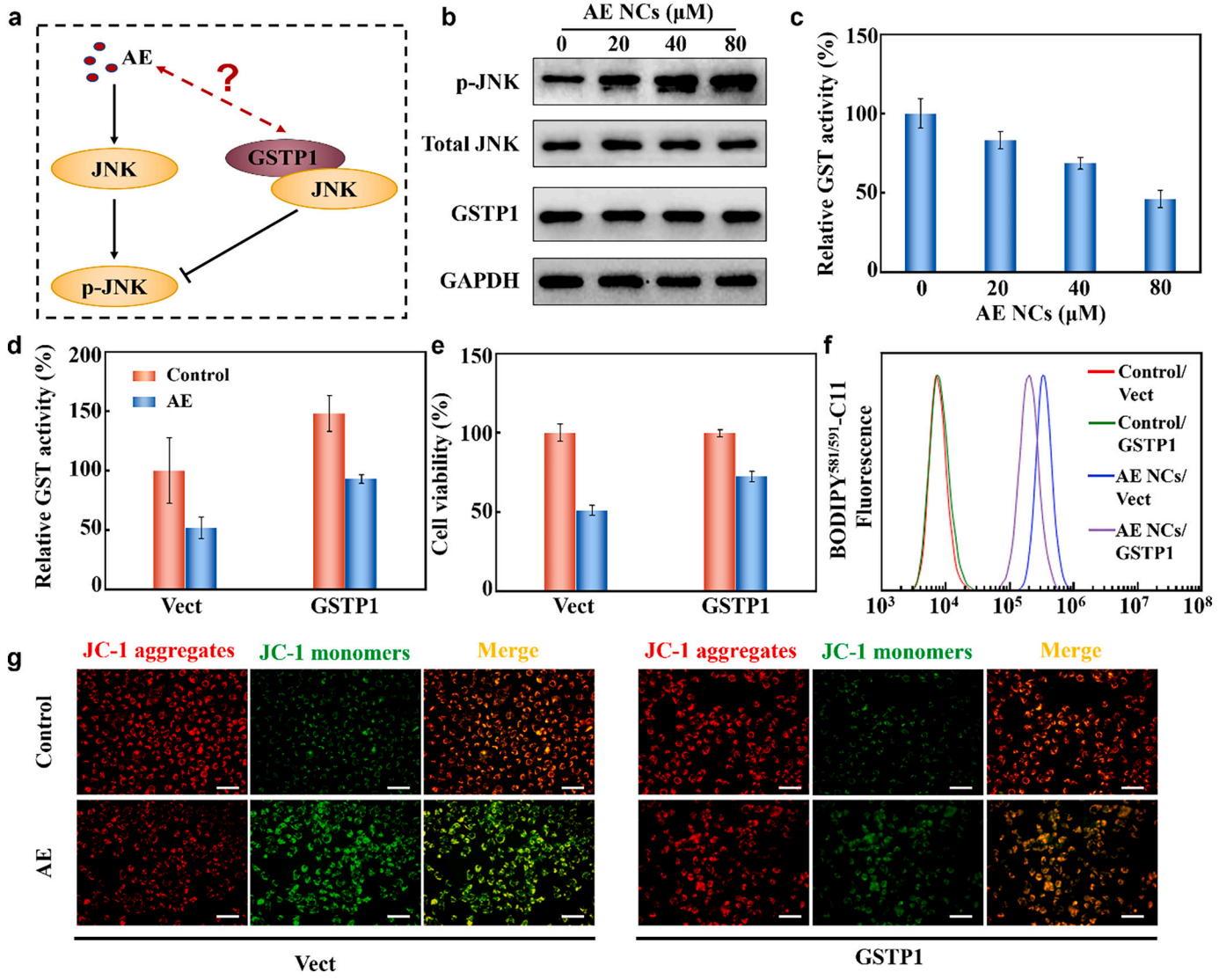

Fig. 4. Activation mechanism of AE-induced ferroptosis. (a) Schematic illustration of the activation and inhibition of JNK by AE and GSTP1, respectively. (b) Western blot analysis of p-JNK, JNK and GSTP1 expression in HSC-3 cells after the treatment with different concentrations of AE NCs. (c) Relative activity of GSTP1 with the treatment of different concentrations of AE NCs ($n = 3$). (d) Intracellular GSTP1 activity in HSC-3 cells after AE NCs (40 μM) treatment, with no treatment as control ($n = 3$). (e) Cell viability of HSC-3 cells after AE NCs (40 μM) treatment ($n = 3$). (f) Flow cytometry assay of cellular LPO by BODIPY$^{581/591}$-C11 staining after AE NCs (40 μM) treatment. (g) Mitochondria membrane potential analysis by JC-1 staining after AE NCs (40 μM) treatment (Scale bar: 50 μm).

extracellular oxygen depletion assay kit to verify the oxygen supply capacity of AE@RBC/Fe NCs. As shown in Fig. 5a, the ferritin-containing formulation greatly reduced the phosphorescence signal compared to other formulations due to the triplet-state quench of the probe by oxygen. This evidence suggests that AE@RBC/Fe NCs exhibit a significant ability to increase oxygen supply. After evaluating the oxygen-evolving ability of AE@RBC/Fe NCs, the intracellular ROS production was examined by DCFH-DA, a ROS sensor that would emit green fluorescence when reacted with ROS [21]. Fluorescence microscope observation and flow cytometry quantification showed that all formulations produced green fluorescence of various intensities compared with the control group (PBS treated) in the absence of laser radiation (Fig. 5b and c). This can be interpreted as AE-induced ferroptosis generating lethal LPO, a typical ROS. The AE@RBC/Fe NCs treated cells produced stronger green fluorescence than the AE NCs treated cells, indicating that the integration of ferritin promoted the extent of cellular ferroptosis, which was consistent with Fig. 3. Once HSC-3 cells were treated with AE@RBC/Fe NCs and then exposed to laser irradiation, their fluorescent signal increased dramatically, suggesting that AE can act as a photosensitizer to generate $^1O_2$ to further replenish ROS. Not negligibly the release of Fe^{3+} from ferritin can provide sufficient oxygen supply for AE-mediated PDT. In addition, the production ability of ROS induced by free AE and AE NCs treated HSC-3 cells was also significantly enhanced in the presence of laser irradiation (Fig. S14). These results clearly confirm that AE@RBC/Fe NCs accumulates ROS in the cells *via* both ferroptosis and PDT pathways.

Since AE@RBC/Fe NCs exhibited superior ROS generation and cellular uptake, we further evaluated the cytotoxicity of different formulations in HSC-3 cells by standard MTT assay. As shown in Fig. 5d, both free AE and AE NCs exhibited a limited decrease in cell viability after treatment with higher drug concentrations. However, AE NCs exhibited more pronounced proliferation inhibition than free AEs, which can be explained by the fact that AE NCs are more soluble leading to higher drug concentration around the cells [19]. Overall, the cell viability was high in both the free AE and AE NCs-treated groups at lower doses, but cell viability was significantly reduced when equal doses of AE@RBC/Fe NCs were treated, consistent with the results for ROS production (Fig. 5b and c). Cytotoxicity in HSC-3 cells increased

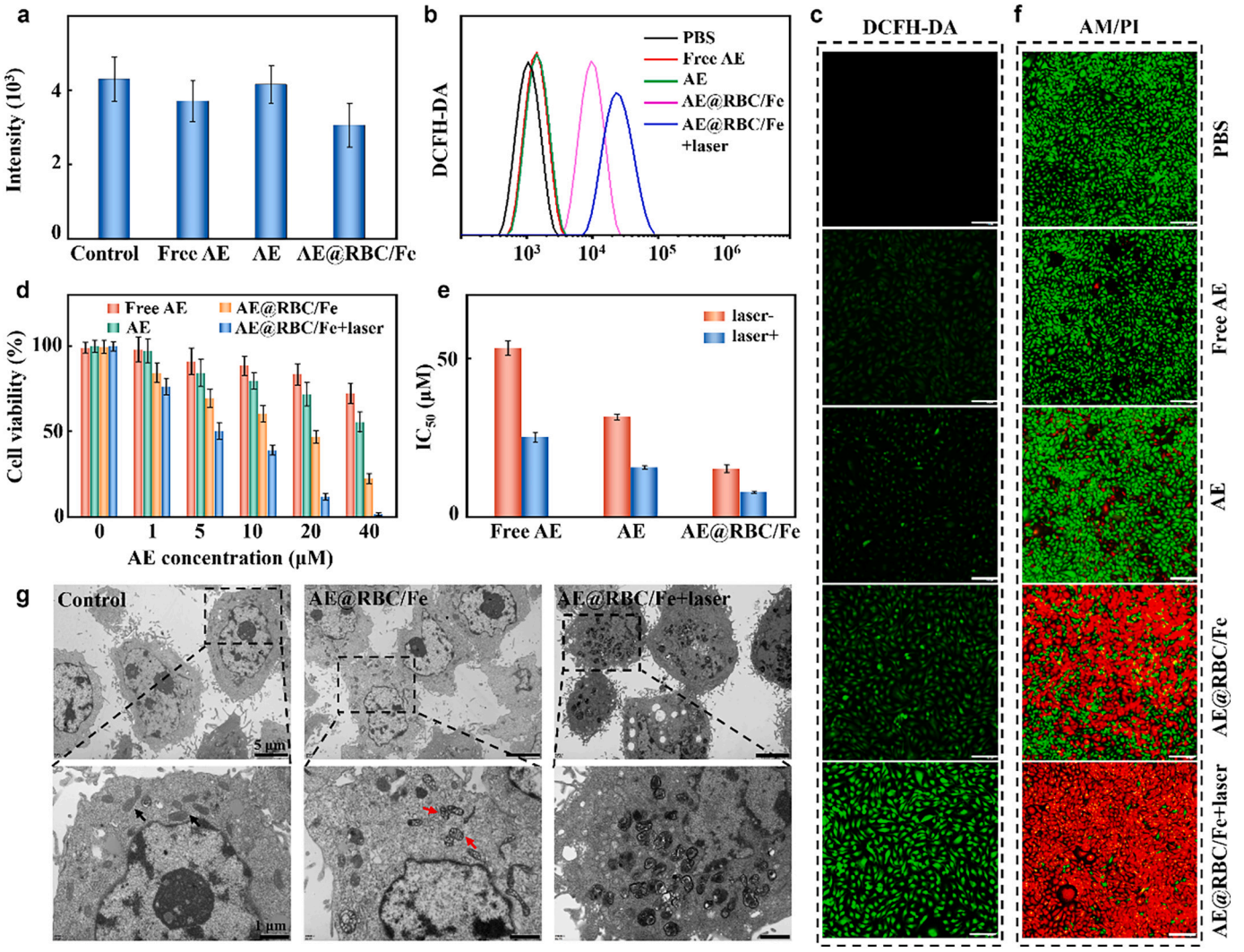

Fig. 5. Cytotoxicity of AE@RBC/Fe NCs in HSC-3 cells. (a) Phosphorescence intensity of the oxygen probe reflecting dissolved oxygen in the culture medium of HSC-3 cells after treated with different formulations ($n = 5$). (b) Flow cytometry analysis and (c) fluorescence images (Scale bar: 100 μm) of DCFH-DA stained HSC-3 cells after different treatments. (d) Cell viability of HSC-3 cells after different treatments ($n = 5$). (e) IC_{50} summary of different treatments ($n = 5$). (f) Live/dead staining assay of HSC-3 cells by Calcein AM (green) and PI (red) after different treatments (Scale bar: 200 μm). (g) TEM images of HSC-3 cells after different treatments, with cells without treatment as control. Black arrow: normal mitochondria, red arrow: damaged mitochondria. (For interpretation of the references to color in this figure legend, the reader is referred to the web version of this article.)

with increasing AE@RBC/Fe NCs concentration, with cell viability decreasing to 22.5% at drug concentration of 40 μM. This encouraging result suggests that the involvement of ferritin favors the anti-cancer effect of AE@RBC/Fe NCs. More importantly, AE@RBC/Fe NCs incubated with HSC-3 cells under laser radiation exhibited higher cytotoxicity, which validating the efficient antitumor effect of the combination of AE-based ferroptosis and PDT. The results in Fig. S15 similarly indicated that laser radiation enhances the anti-cancer effects of both free AE and AE NCs. Fig. 5e shows a significant difference in the half maximal inhibitory concentration (IC_{50}) of free AE, AE NCs and AE@RBC/Fe NCs. Under laser-on conditions, the IC_{50} of AE@RBC/Fe NCs was 7.8 μM, which was around 3.2 and 2.0-fold lower than that of free AE (25.2 μM) and AE NCs (15.6 μM).

To verify the *in vitro* anti-cancer effect of AE@RBC/Fe NCs more visually, we further used live/dead staining assay to observe the cell status after AE@RBC/Fe NCs treatment. As shown in Fig. 5f, only sporadically distributed dead cells (red signals) were found in the free AE and AE NCs groups compared to the control group, but more cell death was induced when cells were treated with AE@RBC/Fe NCs. Maximum killing of cancer cells was found when AE@RBC/Fe NCs were treated with laser radiation concurrently, which was consistent with the results of the MTT assay (Fig. 5d). In addition, the laser radiation also had a significant effect on the live/dead staining results of free AE and AE NCs-treated cells, and these results suggest that laser radiation is a strong contributor to AE@RBC/Fe NCs lethality for cancer cells (Fig. S16). The apoptosis analysis was consistent with the superior toxicity of AE@RBC/Fe NCs under laser irradiation compared to the other groups (Fig. S17). As expected, AE@RBC/Fe NCs treatment followed by laser radiation resulted in the highest total apoptotic cells including early and late apoptotic cells at approximately 76.51%.

To investigate the effects of PDT, ferroptosis and combined therapies on cell morphology, bio-TEM observations were carried out. As shown in Fig. 5g, control cells without any treatment showed normal cell morphology and their linear or granular mitochondria maintain intact bilayer membrane structure. But AE@RBC/Fe NCs treated cells showed shrunken mitochondria and reduced mitochondrial cristae, which were typical for ferroptosis [2]. Once the AE@RBC/Fe NCs treated group was irradiated with laser, the cells exhibited the dual morphological features of apoptosis and ferroptosis. In addition to the contraction and rupture of mitochondria, which represent the characteristic features of

ferroptosis, distinct chromatin condensation and large vacuoles, which are typical morphological changes of apoptosis [50], could be observed in HSC-3 cells. These results clearly confirm that AE@RBC/Fe NCs can induce ferroptosis and further achieve a more effective synergistic effect of apoptosis and ferroptosis when combined with PDT.

3.7. *In vivo* pharmacokinetics and tumor imaging

Since RBC membrane contains many natural 'self-markers', including CD47 protein, various membrane proteins, glycans, acidic silicon-based molecules, *etc.*, on their surface, RBC membrane-modified nanoparticles are resistant to uptake by the reticuloendothelial system (RES), allowing the nanoparticles to evade immunogenic clearance [51]. RBC membrane is therefore considered to be an ideal material for

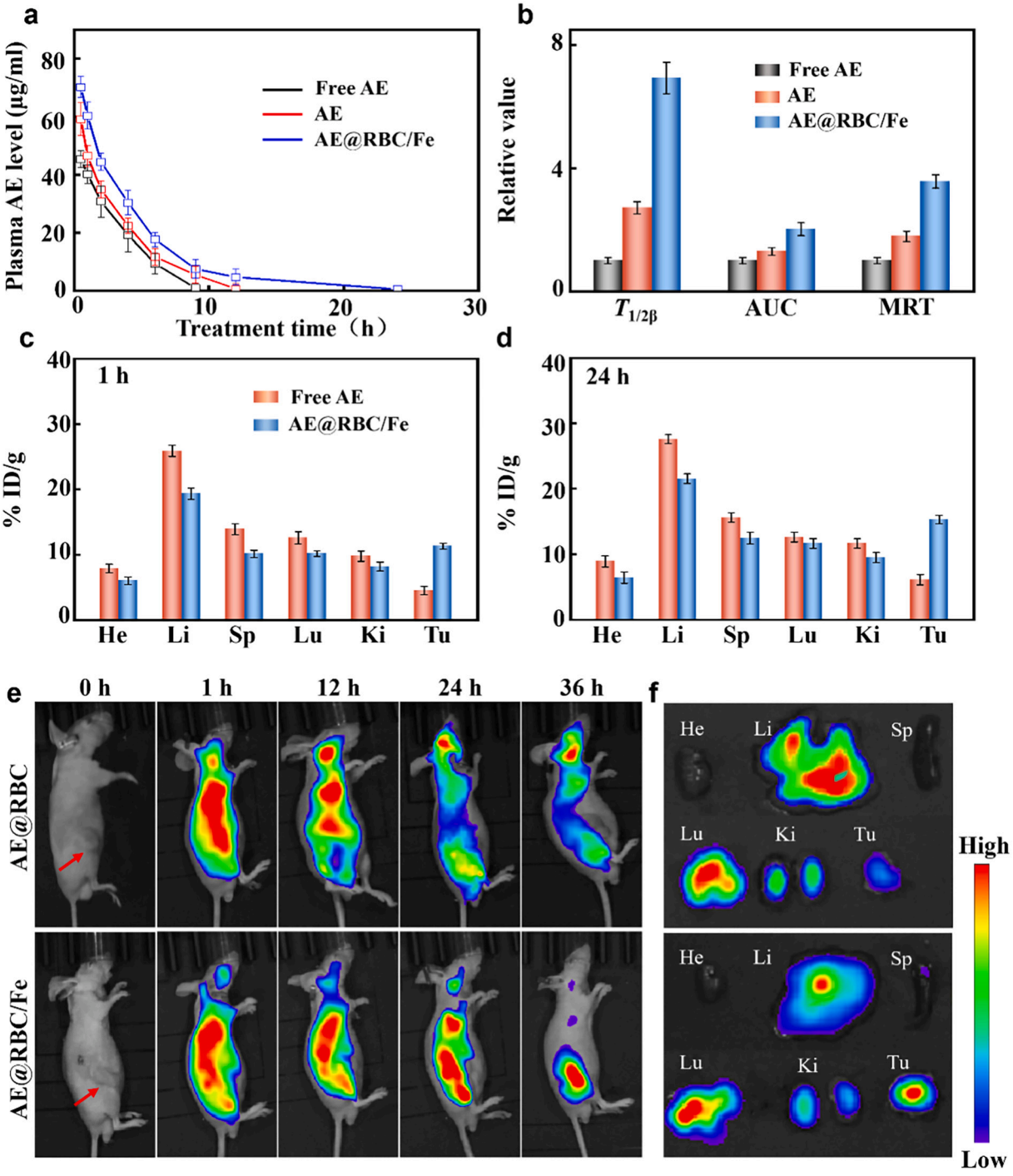

Fig. 6. Pharmacokinetic profile and tissue distribution of AE@RBC/Fe NCs. (a) Plasma AE level along time in mice intravenously injected with free AE, AE NCs and AE@RBC/Fe NCs ($n = 3$). (b) Pharmacokinetic parameters normalization ($n = 3$). (c) AE distribution in the major organs and tumors at 1 h and (d) 24 h after intravenous administration of free AE and AE@RBC/Fe NCs into tumor-bearing mice ($n = 3$). (e) *In vivo* fluorescence images of tumor-bearing mice after intravenous injection with Cy5.5 labeled AE@RBC NCs and AE@RBC/Fe NCs for various time intervals. (f) *Ex vivo* fluorescence images of major organs and tumors at 24 h post-injection. He: heart; Li: liver; Sp: spleen; Lu: lung; Ki: kidney; Tu: tumor.

nanoparticles surface modification in the field of biomimetic design. The pharmacokinetic behavior of RBC membrane-camouflaged AE@RBC/Fe NCs were assessed in Sprague Dawley rats and compared with AE NCs and free AE. As shown in Fig. 6a, all samples exhibited a rapid distribution phase and a slow elimination phase. Compared to free AE which was quickly cleared from the circulation, plasma AE decreased more slowly after AE NCs and AE@RBC/Fe NCs were administrated and AE@RBC/Fe NCs had the longest elimination half-life ($T_{1/2\beta}$) of 9.7 h, 6.9 and 2.5 times longer than that of free AE and AE NCs, respectively. In addition, AE@RBC/Fe NCs administration showed a larger total area under the plasma concentration-time curve from zero to infinity ($AUC_{0-\infty}$) and a longer mean residence time (MRT) compared to free AE and AE

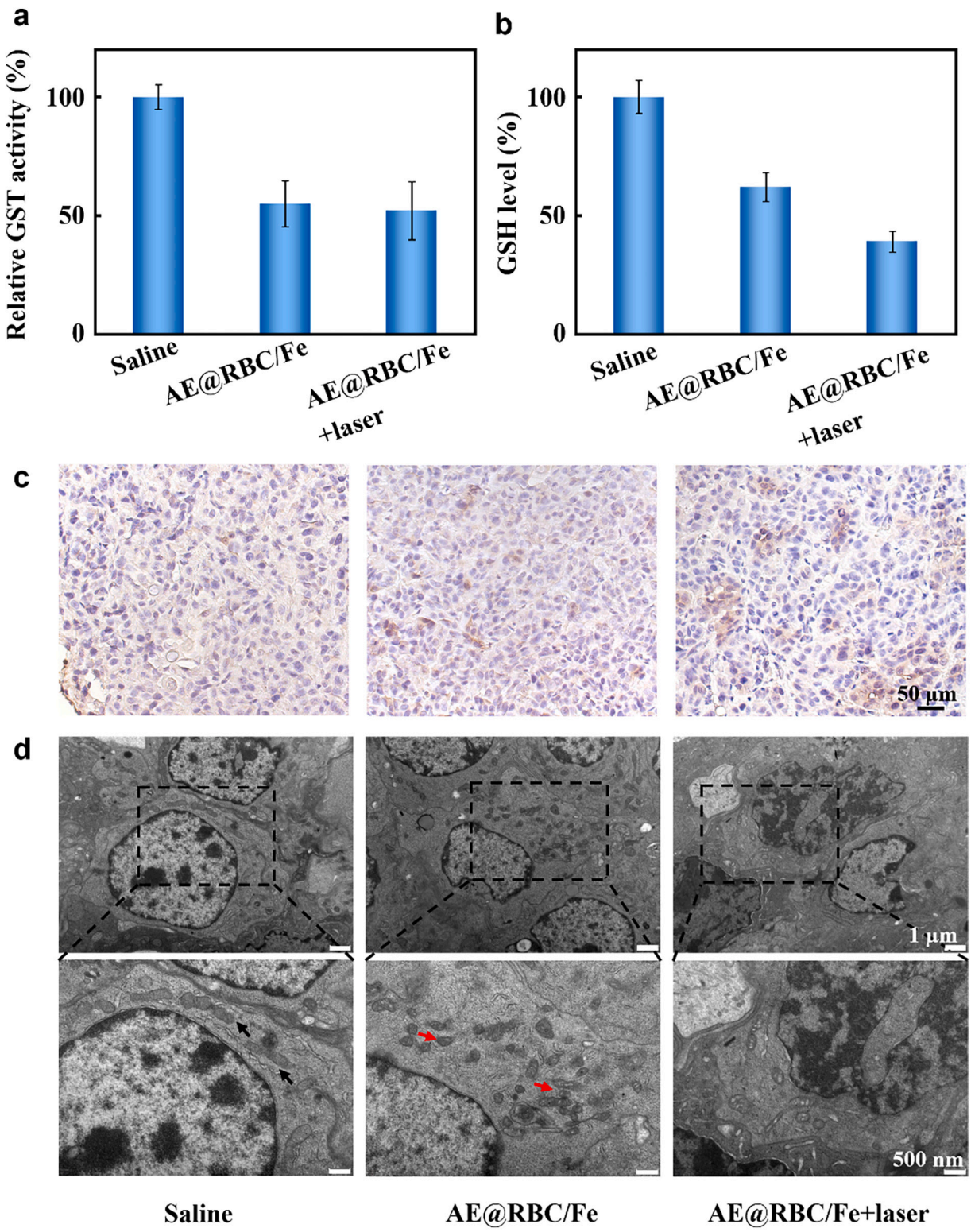

Fig. 7. Verification of the ferroptosis promoted by PDT *in vivo*. (a) GSTP1 activity and (b) GSH level of tumor tissue after different treatments ($n = 3$). (c) IHC staining images of 4-HNE of tumor tissue after different treatments. (d) TEM images of tumor tissue after different treatments. Black arrow: normal mitochondria, red arrow: damaged mitochondria. (For interpretation of the references to color in this figure legend, the reader is referred to the web version of this article.)

NCs. (Fig. 6b). This result suggests that AE NCs coated with RBC membranes offer high bioavailability and significantly extended circulation time.

Tumor-bearing Balb/c nude mice were used to study the *in vivo* distribution of drugs in tumors and major organs by intravenous injection of free AE and AE@RBC/Fe NCs. As shown in Fig. 6c, there was a wide distribution of the drug in the body after injection for 1 h. The higher accumulation in the liver and kidney in comparison to other organs can be explained by the preferential accumulation of the drug in the reticuloendothelial system and the rapid clearance of the drug in the blood by the kidney [52]. In addition, modification of RBC membranes and ferritin on the surface of AE NCs could further improve blood retention and tumor targeting thereby improving the accumulation of AE in tumor tissue. There was a significant difference in AE distribution after 24 h of administration, where AE levels in AE@RBC/Fe NCs treated tumors were approximately 2.5 times higher compared to that injected with free AE (Fig. 6d).

Precise tumor targeting performance is a key factor for effective tumor treatment and reduced side-effects, therefore we further explored the real-time distribution of the drug with Cy5.5-labeled AE@RBC/Fe NCs *in vivo* using an *in vivo* animal imaging system. As shown in Fig. 6e, the fluorescent signal of Cy5.5 was rapidly and widely distributed *in vivo* after intravenous injection of AE@RBC NCs and AE@RBC/Fe NCs. As the drug cycle time increased, the AE@RBC/Fe NCs-treated nude mice showed the strongest fluorescence signal at 24 h at the tumor site, in contrast to the AE@RBC NCs treatment group where the fluorescence signal almost disappeared, further confirming the better tumor homing ability of the modified ferritin. Furthermore, *ex vivo* fluorescence imaging of tumors and major organs obtained 24 h after injection showed that tumor sites in mice treated with AE@RBC/Fe NCs exhibited a much higher fluorescence intensity than the organs (Fig. 6f). These results clearly indicate that the RBC membrane wrapping and ferritin modification strategy allows for the full accumulation of AE@RBC/Fe NCs at the tumor site.

3.8. AE@RBC/Fe NCs inducing enhanced ferroptosis by PDT

To deeply investigate the synergistic antitumor mechanism of AE@RBC/Fe NCs *in vivo*, the extent of ferroptosis produced by AE@RBC/Fe NCs before and after PDT treatment was examined. We first investigated the effect of AE@RBC/Fe NCs on GSTP1 activity, and the results showed that GSTP1 activity was significantly decreased after AE@RBC/Fe NCs treatment (Fig. 7a), which was consistent with the results of *in vitro* experiments. Considering that GSTP1 can inhibit the phosphorylation/activation of JNK by binding to JNK, it was verified whether AE@RBC/Fe NCs treatment affected the phosphorylation/activation of JNK. As shown in Fig. S18, substrate phosphorylation/activation of JNK was triggered by AE@RBC/Fe NCs treatment on the basis of unchanged total JNK. Interestingly, the involvement of PDT further increased the phosphorylation/activation of JNK, probably due to the activation of the ROS/JNK signaling pathway by PDT [53]. As shown in Fig. 7b, AE@RBC/Fe NCs resulted in a significant decrease of GSH levels in tumor tissues compared with the control group (saline), and the depletion of GSH was further exacerbated by PDT treatment. The expression level of MDA, an advanced lipoxidation end-product, is elevated throughout ferroptosis [54]. The results of MDA assay showed elevated MDA levels in the AE@RBC/Fe NCs and AE@RBC/Fe NCs + laser groups, and PDT treatment further increased MDA accumulation, which was negatively correlated with changes in GSH levels (Fig. S19). We next assessed another marker of lipid peroxidation, 4-HNE, whose overexpression is a key feature of ferroptosis [55]. Fig. 7c shows a similar trend of tumor ferroptosis observed by IHC staining of 4-HNE. After treatment with "AE@RBC/Fe NCs + laser", the percentage of 4-HNE positive cells was higher than the single treatment with AE@RBC/Fe NCs. Mitochondria are the main hub for iron accumulation, therefore the morphological changes of mitochondria reflect the distinction between ferroptosis and other forms of cell death [56]. As shown in Fig. 7d, mitochondrial damage associated with morphology of ferroptosis (mitochondrial shrinkage and volume reduction) can be observed in AE@RBC/Fe NCs treated tumor by bio-TEM [2]. Notably, tumor cells treated with laser irradiation exhibited dual morphological features of ferroptosis and apoptosis including smaller mitochondria with distinct chromatin condensation. In conclusion, the levels of GSH and LPO in tumor tissues, as well as changes in mitochondrial morphology, suggested that AE@RBC/Fe NCs induce ferroptosis *in vivo* by inhibiting GSTP1 activity. All the above results also indicated that PDT can further enhance AE@RBC/Fe NCs-induced ferroptosis by increased LPO, as PDT elevated intracellular ROS levels and depressed GSH levels [57].

3.9. In vivo antitumor efficacy of AE@RBC/Fe NCs

Based on the excellent tumor targeting and efficient tumor cell inhibition effect of AE@RBC/Fe NCs, the synergistic therapeutic effect of AE@RBC/Fe NCs *in vivo* was further explored by evaluating the tumor growth, animal survival and histopathological examination. *In vivo* imaging results showed a gradual accumulation of AE@RBC/Fe NCs in the cancer site after injection, with a peak at 24 h (Fig. 6e). Based on these results, a time point of 24 h post-injection was chosen for the administration of robust PDT in subsequent experiments to achieve the optimal synergistic therapeutic effect. As shown in Fig. 8a, mice randomly divided into five groups were treated intravenously with the appropriate formulations and assessed for tumor size change at preestablished time points. Tumor volume measurements showed a slight inhibition by free AE and AE NCs compared to the saline group, and their tumors grew rapidly to approximately 840 and 713 mm^3 after 21 days of treatment. In contrast, the AE@RBC/Fe NCs effectively inhibited tumor growth, especially when the mice were exposed to 405 nm irradiation, showing the best antitumor effect both in terms of tumor volume data and representative pictures (Fig. 8b). The progression of tumor volume in the AE@RBC/Fe NCs group with laser was negligible and the inhibition ratio was demonstrated to be as high as 95.8%. In addition, to further monitor the survival rate of the animals, the number of live animals at different time points was recorded. Kaplan-Meier plots of animal survival as shown in Fig. 8c showed a general prolongation of survival time after treatment with all formulations compared to the saline treatment (median survival time was 16 days). The group of "AE@RBC/Fe NCs + laser" exhibited the most significant prolongation of animal survival with a median survival time of 35 days.

In addition, the tumors were retrieved after 21 days of treatment to further study the microcosmic therapeutic efficacy by the pathological examination toward tumor slices. As shown in Fig. 8d, the AE@RBC/Fe NCs-treated tumor cells showed significant vacuolar degeneration, with a certain number of cells in a necrotic state, and the largest area of necrosis in the group with laser irradiation. In contrast, in the free AE and AE NCs treated groups, most of the tumor cells remained intact and the cell killing effect in the free AE group in particular was negligible. A similar trend of tumor proliferation and apoptosis was observed by IHC staining for Ki-67 and Caspase-3. The percentage of Ki-67 positive cells was significantly lower in the synergistic treatment group "AE@RBC/Fe NCs + laser" (7.7%) compared to free AE (81.6%), AE NCs (63.2%) and AE@RBC/Fe NCs (31.9%) single treatments. After treatment with "AE@RBC/Fe NCs + laser", Caspase-3 positive cells was around 83.3%, which was much higher than those of free AE (16.5%), AE NCs (44.8%) and AE@RBC/Fe NCs (60.2%) single treatments. All these results clearly demonstrate the superior anticancer efficacy of our designed system combining PDT and ferroptosis.

3.10. In vivo toxicity of AE@RBC/Fe NCs treatment

Nanoparticles may cause biochemical changes *in vivo*, which in turn causing abnormal responses in the blood and tissues. The overall health

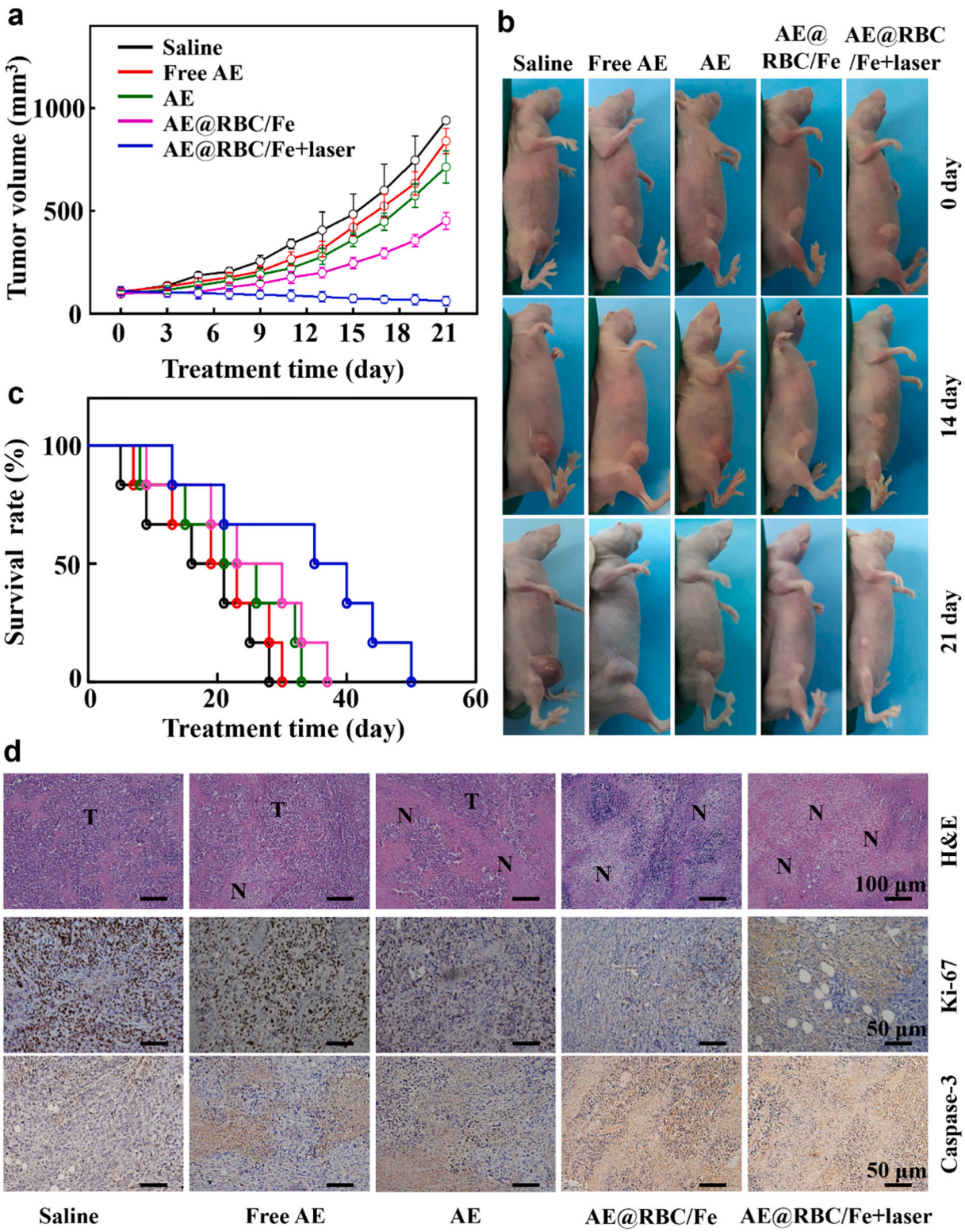

Fig. 8. Antitumor efficacy of AE@RBC/Fe NCs. (a) Variations of tumor volume and (b) representative photographs of tumor-bearing mice after various treatments at different time intervals ($n = 6$). (c) Survival rate of tumor-bearing mice after different treatments, with saline injection as control ($n = 6$). (d) Typical H&E staining ('N' represents necrotic areas) and IHC staining images of Ki-67 and Caspase-3 of tumors retrieved after 21 days of different treatments.

status of the animals can be measured by a simple and reliable method of measuring body weight. As shown in Fig. S20, the body weight of the mice in each treatment group remained virtually unchanged over the 21-day treatment period. Blood routine examination reflected bone marrow function and non-specific immune interactions, and the results of whole blood count analysis showed no significant changes in major index, such as RBC, WBC, PLT, HGB in the AE@RBC/Fe NCs treated and control groups. In addition, serum biochemical parameters related to liver and kidney function (AST, ALP, ALT and BUN) were only marginally different after treatment compared to the control group (Fig. S21). The

major organs of the mice were examined histologically by H&E staining. As shown in Fig. S22, there was no significant pathological abnormalities in the heart, liver, spleen, kidney and lung in the treated mice compared to the PBS control group, indicating the favorable biocompatibility of AE@RBC/Fe NCs.

4. Conclusion

In summary, an anthraquinone derivative AE with ferroptosis activator and photosensitizer properties was searched to fabricate a biomimetic AE@RBC/Fe NCs for synergetic cancer therapy. We unexpectedly found that the triggering mechanism of AE-induced ferroptosis was not the well-understood down-regulated expression of GPX4, but rather specifical inhibition of GSTP1 activity. The introduction of ferritin not only provides tumor targeting for AE@RBC/Fe NCs, but also serves as an iron pool for sustained release of Fe^{3+}, and thus enhancing the inhibition of tumor proliferation by ferroptosis and PDT. Furthermore, given the biomimetic modification of AE NCs core by the RBC membrane, AE@RBC/Fe NCs can escape immune clearance *in vivo* and significantly improve its tumor accumulation. More importantly, this nanoplatform is simple to prepare and clever to integrate photosensitizer and ferroptosis activator into one single subject, facilitating the practical translation of ferroptosis and PDT synergistic therapy strategies. As a novel antitumor nanoplatform, AE@RBC/Fe NCs can functionally combine the PDT-induced apoptosis and non-apoptotic ferroptosis to achieve superior therapeutic effects than free AE. However, the maximum absorption band of AE is in the blue region, making AE mediated PDT only advantageous for the treatment of superficial diseases such as skin cancer, oral cavity and eye diseases. This also inspires us that future research should not only focus on the therapeutic effects of photosensitizer nanocrystals, but also address the limitations of their application to deep tumors.

CRediT authorship contribution statement

Mingbo Wu: Conceptualization, Methodology, Validation, Formal analysis, Investigation, Writing – original draft, Visualization, Writing – review & editing. **Wenwu Ling:** Investigation, Methodology, Validation, Formal analysis. **Jiaojun Wei:** Conceptualization, Methodology, Validation, Formal analysis, Investigation, Writing – review & editing. **Ran Liao:** Visualization, Writing – review & editing. **Haiyue Sun:** Investigation. **Dongqiu Li:** Investigation. **Ye Zhao:** Writing – review & editing. **Long Zhao:** Conceptualization, Validation, Formal analysis, Writing – original draft, Writing – review & editing, Supervision.

Data availability

All data included in this study are available upon request by contact with the corresponding author.

Acknowledgements

This work is supported by the National Natural Science Foundation of China (51803015, 81902786 and 31701212), the Scientific Research Foundation of Science & Technology Department of Sichuan Province (2021ZYD0067 and 2020YJ0371), the Chengdu Science and Technology Innovation R&D Project (2021-YF05-01518-SN and 2021-YF05-00818-SN), the Fundamental Research Funds for Central Universities (2022SCU12032), the Special Project of Liyan Workshop Aesthetic Medicine Research Center of Chengdu Medical College (20YM005), the Scientific Research Foundation of Development and Regeneration Key Lab of Sichuan Province (SYS22-08).

Appendix A. Supplementary data

Supplementary data to this article can be found online at https://doi.org/10.1016/j.jconrel.2022.11.026.

References

[1] J.P.F. Angeli, D.V. Krysko, M. Conrad, Ferroptosis at the crossroads of cancer-acquired drug resistance and immune evasion, Nat. Rev. Cancer 19 (2019) 405–414.
[2] S.J. Dixon, K.M. Lemberg, M.R. Lamprecht, R. Skouta, E.M. Zaitsev, C.E. Gleason, D.N. Patel, A.J. Bauer, A.M. Cantley, W.S. Yang, B. Morrison, B.R. Stockwell, Ferroptosis: an iron-dependent form of nonapoptotic cell death, Cell 149 (2012) 1060–1072.
[3] B. Lu, X.B. Chen, M.D. Ying, Q.J. He, J. Cao, B. Yang, The role of ferroptosis in cancer development and treatment response, Front. Pharmacol. 8 (2018) 992.
[4] Y. Xie, W. Hou, X. Song, Y. Yu, J. Huang, X. Sun, R. Kang, D. Tang, Ferroptosis: process and function, Cell Death Differ. 23 (2016) 369–379.
[5] D.W. Zheng, Q. Lei, J.Y. Zhu, J.X. Fan, C.X. Li, C. Li, Z.S. Xu, S.X. Cheng, X. Z. Zhang, Switching apoptosis to ferroptosis: metal-organic network for high-efficiency anticancer therapy, Nano Lett. 17 (2017) 284–291.
[6] L. Ding, X. Lin, Z.G. Lin, Y.N. Wu, X.L. Liu, J.F. Liu, M. Wu, X.L. Zhang, Y.Y. Zeng, Cancer cell-targeted photosensitizer and therapeutic protein co-delivery nanoplatform based on a metal-organic framework for enhanced synergistic photodynamic and protein therapy, ACS Appl. Mater. Interfaces 12 (2020) 36906–36916.
[7] J.L. Gao, H.G. Zhou, Y.J. Zhao, L. Lu, J.Z. Zhang, W.T. Cheng, X.X. Song, Y. X. Zheng, C.Y. Chen, J.L. Tang, Time-course effect of ultrasmall superparamagnetic iron oxide nanoparticles on intracellular iron metabolism and ferroptosis activation, Nanotoxicology 15 (2021) 366–379.
[8] H.L. Cheng, X.Y. Wang, X. Liu, X. Wang, H. Wen, Y.K. Cheng, A.J. Xie, Y.H. Shen, R. P. Tang, M.Z. Zhu, An effective NIR laser/tumor-microenvironment co-responsive cancer theranostic nanoplatform with multi-modal imaging and therapies, Nanoscale 13 (2021) 10816–10828.
[9] L.X. Zang, H.M. Zhao, X.Y. Ji, W.W. Cao, Z.G. Zhang, P.S. Meng, Photophysical properties, singlet oxygen generation efficiency and cytotoxic effects of aloe emodin as a blue light photosensitizer for photodynamic therapy in dermatological treatment, Photochem. Photobiol. Sci. 16 (2017) 1088–1094.
[10] Y. Wang, J. Li, S.M. Geng, X.P. Wang, Z.X. Cui, W.P. Ma, M. Yuan, C.C. Liu, Y.H. Ji, Aloe-emodin-mediated antimicrobial photodynamic therapy against multidrug-resistant acinetobacter baumannii: an in vivo study, Photodiagn. Photodyn. Ther. 34 (2021), 102311.
[11] X.X. Dong, B.R. Ni, J. Fu, X.B. Yin, L.T. You, X. Leng, X. Liang, J. Ni, Emodin induces apoptosis in human hepatocellular carcinoma HepaRG cells via the mitochondrial caspase-dependent pathway, Oncol. Rep. 40 (2018) 1985–1993.
[12] G.D. Lu, H.-M. Shen, M.C.M. Chung, C.N. Ong, Critical role of oxidative stress and sustained JNK activation in aloe-emodin-mediated apoptotic cell death in human hepatoma cells, Carcinogenesis 28 (2007) 1937–1945.
[13] X. Wang, X. Xin, Y. Sun, L.Z. Zou, H. Li, Y.F. Zhao, R.H. Li, Y. Peng, J. Zheng, Chemical reactivity of aloe-emodin and its hydroxylation metabolites to thiols, Chem. Res. Toxicol. 32 (2019) 234–244.
[14] W. Hou, Y.C. Xie, X.X. Song, X.F. Sun, M.T. Lotze, H.J. Zeh, R. Kang, D.L. Tang, Autophagy promotes ferroptosis by degradation of ferritin, Autophagy 12 (2016) 1425–1428.
[15] X.Y. Wang, M. Wu, X.L. Zhang, F.D. Li, Y.Y. Zeng, X.Y. Lin, X.L. Liu, J.F. Liu, Hypoxia-responsive nanoreactors based on self-enhanced photodynamic sensitization and triggered ferroptosis for cancer synergistic therapy, J. Nanobiotechnol. 19 (2021) 204.
[16] M.M. Liang, K.L. Fan, M. Zhou, D.M. Duan, J.Y. Zheng, D.L. Yang, J. Feng, X. Y. Yan, H-ferritin-nanocaged doxorubicin nanoparticles specifically target and kill tumors with a single-dose injection, Proc. Natl. Acad. Sci. U. S. A. 111 (2014) 14900–14905.
[17] D.E. Johnson, B. Burtness, C.R. Leemans, V.W.Y. Lui, J.E. Bauman, J.R. Grandis, Head and neck squamous cell carcinoma, Nat. Rev. Dis. Prim. 6 (2020) 92.
[18] S. Hosokawa, G. Takahashi, K.I. Sugiyama, S. Takebayashi, J. Okamura, Y. Takizawa, H. Mineta, Porfimer sodium-mediated photodynamic therapy in patients with head and neck squamous cell carcinoma, Photodiagn. Photodyn. Ther. 29 (2020), 101627.
[19] M.S. Freag, Y.S.R. Elnaggar, D.A. Abdelmonsif, O.Y. Abdallah, Stealth, biocompatible monoolein-based lyotropic liquid crystalline nanoparticles for enhanced aloe-emodin delivery to breast cancer cells: in vitro and in vivo studies, Int. J. Nanomedicine 11 (2016) 4799–4818.
[20] I. Kim, Y. Kim, S.W. Lee, D. Lee, H.G. Jung, J.W. Jang, T. Lee, Y.K. Yoon, G. Lee, D. S. Yoon, Erythrocyte-camouflaged biosensor for alpha-hemolysin detection, Biosens. Bioelectron. 185 (2021), 113267.
[21] L. Zhao, Z.X. Li, J.J. Wei, Y. Xiao, Y. She, Q.X. Su, T. Zhao, J.Y. Li, J.C. Shao, Juglone-loaded metal-organic frameworks for H_2O_2 self-modulating enhancing chemodynamic therapy against prostate cancer, Chem. Eng. J. 430 (2022), 133057.
[22] Y. Wang, K. Zhang, X. Qin, T.H. Li, J.H. Qiu, T.Y. Yin, J.L. Huang, S. McGinty, G. Pontrelli, J. Ren, Q.W. Wang, W. Wu, G.X. Wang, Biomimetic nanotherapies: red blood cell based core-shell structured nanocomplexes for atherosclerosis management, Adv. Sci. 6 (2019), 1900172.
[23] L. Liu, X. Bai, M.V. Martikainen, A. Kårlund, M. Roponen, W. Xu, G. Hu, E. Tasciotti, V.P. Lehto, Cell membrane coating integrity affects the internalization mechanism of biomimetic nanoparticles, Nat. Commun. 12 (2021) 5726.

[24] S. Gao, G.H. Wang, Z.N. Qin, X.Y. Wang, G.Q. Zhao, Q.J. Ma, L. Zhu, Oxygen-generating hybrid nanoparticles to enhance fluorescent/photoacoustic/ultrasound imaging guided tumor photodynamic therapy, Biomaterials 112 (2017) 324–335.
[25] C.H.A. Boalwe, K. Patel, M. Singh, Doxorubicin liposomes as an investigative model to study the skin permeation of nanocarriers, Int. J. Pharm. 489 (2015) 106–116.
[26] L. Lin, Y. Dai, H. Cui, Antibacterial poly(ethylene oxide) electrospun nanofibers containing cinnamon essential oil/beta-cyclodextrin proteoliposomes, Carbohydr. Polym. 178 (2017) 131–140.
[27] T. Liu, W. Liu, M. Zhang, W. Yu, F. Gao, C. Li, S.B. Wang, J. Feng, X.Z. Zhang, Ferrous-supply-regeneration nanoengineering for cancer-cell-specific ferroptosis in combination with imaging-guided photodynamic therapy, ACS Nano 12 (2018) 12181–12192.
[28] W. Feng, X.G. Han, H. Hu, M.Q. Chang, L. Ding, H.J. Xiang, Y. Chen, Y.H. Li, 2D vanadium carbide MXenzyme to alleviate ROS-mediated inflammatory and neurodegenerative diseases, Nat. Commun. 12 (2021) 2203.
[29] Z.W. Zhou, H. Wu, R.X. Yang, A. Xu, Q.Y. Zhang, J.W. Dong, C.G. Qian, M.J. Sun, GSH depletion liposome adjuvant for augmenting the photothermal immunotherapy of breast cancer, Sci. Adv. 6 (2020) eabc4373.
[30] Q. Cheng, W.Y. Yu, J.J. Ye, M.D. Liu, W.L. Liu, C. Zhang, C. Zhang, J. Feng, X. Z. Zhang, Nanotherapeutics interfere with cellular redox homeostasis for highly improved photodynamic therapy, Biomaterials 224 (2019), 119500.
[31] Q. Feng, X. Yang, Y. Hao, N. Wang, X. Feng, L. Hou, Z. Zhang, Cancer cell membrane-biomimetic nanoplatform for enhanced sonodynamic therapy on breast cancer via autophagy regulation strategy, ACS Appl. Mater. Interfaces 11 (2019) 32729–32738.
[32] M.A. Goren, T. Morizumi, I. Menon, J.S. Joseph, J.S. Dittman, V. Cherezov, R. C. Stevens, O.P. Ernst, A.K. Menon, Constitutive phospholipid scramblase activity of a G protein-coupled receptor, Nat. Commun. 5 (2014) 5115.
[33] L. Hou, C.Y. Tian, Y.S. Yan, L.W. Zhang, H.J. Zhang, Z.Z. Zhang, Manganese-based nanoactivator optimizes cancer immunotherapy via enhancing innate immunity, ACS Nano 14 (2020) 3927–3940.
[34] T. Krajnovic, D. Maksimovic-Ivanic, S. Mijatovic, D. Draca, K. Wolf, D. Edeler, L. A. Wessjohann, G.N. Kaluderovic, Drug delivery system for emodin based on mesoporous silica SBA-15, Nanomaterials 8 (2018) 322.
[35] Q.F. Chen, X.B. Ma, L. Xie, W.J. Chen, Z.G. Xu, E.Q. Song, X.K. Zhu, Y. Song, Iron-based nanoparticles for MR imaging-guided ferroptosis in combination with photodynamic therapy to enhance cancer treatment, Nanoscale 13 (9) (2021) 4855–4870.
[36] H. Chen, Y. Wan, X. Cui, S. Li, C.S. Lee, Recent advances in hypoxia-overcoming strategy of aggregation-induced emission photosensitizers for efficient photodynamic therapy, Adv. Healthc. Mater. 10 (2021), 2101607.
[37] J. Chen, F. Chen, L. Zhang, Z.Y. Yang, T. Deng, Y.F. Zhao, T.Y. Zheng, X.L. Gan, H. T. Zhong, Y.Q. Geng, X.W. Fu, Y.Q. Wang, C. Yu, Self-assembling porphyrins as a single therapeutic agent for synergistic cancer therapy: a one stone three birds strategy, ACS Appl. Mater. Interfaces 13 (2021) 27856–27867.
[38] Q. Jiang, Y. Liu, R. Guo, X. Yao, S. Sung, Z. Pang, W. Yang, Erythrocyte-cancer hybrid membrane-camouflaged melanin nanoparticles for enhancing photothermal therapy efficacy in tumors, Biomaterials 192 (2019) 292–308.
[39] M. Sun, Y. Duan, Y. Ma, Q. Zhang, Cancer cell-erythrocyte hybrid membrane coated gold nanocages for near infrared light-activated photothermal/radio/chemotherapy of breast cancer, Int. J. Nanomedicine 15 (2020) 6749–6760.
[40] Y. Yu, H.B. Liu, D. Yang, F. He, Y. Yuan, J. Guo, J. Hu, J. Yu, X.Q. Yan, S. Wang, Z. M. Du, Aloe-emodin attenuates myocardial infarction and apoptosis via up-regulating miR-133 expression, Pharmacol. Res. 146 (2019), 104315.
[41] H.J. Kim, J.W. Choi, J. Ree, J.S. Lim, J. Lee, J. Il Kim, S.B. Thapa, J.K. Sohng, Y. Il Park, Aloe emodin 3-O-glucoside inhibits cell growth and migration and induces apoptosis of non-small-cell lung cancer cells via suppressing MEK/ERK and Akt signalling pathways, Life Sci. 300 (2022), 120495.
[42] X.R. Pang, L.L. Shao, X.J. Nie, H.Y. Yan, C. Li, A.J. Yeo, M.F. Lavin, Q. Xia, H. Shao, G.C. Yu, Q. Jia, C. Peng, Emodin attenuates silica-induced lung injury by inhibition of inflammation, apoptosis and epithelial-mesenchymal transition, Int. Immunopharmacol. 91 (2021), 107277.
[43] T. Xu, Y.Y. Ma, Q.L. Yuan, H.X. Hu, X.K. Hu, Z.Y. Qian, J.K. Rolle, Y.Q. Gu, S.W. Li, Enhanced ferroptosis by oxygen-boosted phototherapy based on a 2-in-1 nanoplatform of ferrous hemoglobin for tumor synergistic therapy, ACS Nano 14 (2020) 3414–3425.
[44] Y. Zou, M.J. Palte, A.A. Deik, H.X. Li, J.K. Eaton, W.Y. Wang, Y.Y. Tseng, R. Deasy, M. Kost-Alimova, V. Dancik, E.S. Leshchiner, V.S. Viswanathan, S. Signoretti, T. K. Choueiri, J.S. Boehm, B.K. Wagner, J.G. Doench, C.B. Clish, P.A. Clemons, S. L. Schreiber, A GPX4-dependent cancer cell state underlies the clear-cell morphology and confers sensitivity to ferroptosis, Nat. Commun. 10 (2019) 1617.
[45] X.X. Fang, H. Wang, D. Han, E.J. Xie, X. Yang, J.Y. Wei, S.S. Gu, F. Gao, N.L. Zhu, X.J. Yin, Q. Cheng, P. Zhang, W. Dai, J.H. Chen, F.Q. Yang, H.T. Yang, A. Linkermann, W. Gu, J.X. Min, F.D. Wang, Ferroptosis as a target for protection against cardiomyopathy, Proc. Natl. Acad. Sci. U. S. A. 116 (2019) 2672–2680.
[46] S.S. Li, Y.E. Zhou, Q.X. Huang, X.H. Fu, L. Zhang, F. Gao, Z. Jin, L.M. Wu, C.Y. Shu, X.R. Zhang, W.H. Xu, J. Shu, Iron overload in endometriosis peritoneal fluid induces early embryo ferroptosis mediated by HMOX1, Cell Death Dis. 7 (2021) 355.
[47] B.R. Stockwell, X.J. Jiang, W. Gu, Emerging mechanisms and disease relevance of ferroptosis, Trends Cell Biol. 30 (2020) 478–490.
[48] A. De Luca, L.J. Parker, W.H. Ang, C. Rodolfo, V. Gabbarini, N.C. Hancock, F. Palone, A.P. Mazzetti, L. Menin, C.J. Morton, M.W. Parker, M. Lo Bello, P. J. Dyson, A structure-based mechanism of cisplatin resistance mediated by glutathione transferase P1-1, Proc. Natl. Acad. Sci. U. S. A. 116 (2019) 13943–13951.
[49] H.X. Tang, C.Q. Li, Y. Zhang, H.Y. Zheng, Y. Cheng, J.J. Zhu, X.J. Chen, Z.H. Zhu, J. G. Piao, F.Z. Li, Targeted manganese doped silica nano GSH-cleaner for treatment of liver cancer by destroying the intracellular redox homeostasis, Theranostics 10 (2020) 9865–9887.
[50] S. Bedoui, M.J. Herold, A. Strasser, Emerging connectivity of programmed cell death pathways and its physiological implications, Nat. Rev. Mol. Cell Biol. 21 (2020) 678–695.
[51] X. Zhen, P.H. Cheng, K.Y. Pu, Recent advances in cell membrane-camouflaged nanoparticles for cancer phototherapy, Small 15 (2019), 1804105.
[52] Z.L. Zhang, D.D. Zhang, B. Qiu, W.X. Cao, Y. Liu, Q.J. Liu, X.H. Li, Icebreaker-inspired Janus nanomotors to combat barriers in the delivery of chemotherapeutic agents, Nanoscale 13 (2021) 6545–6557.
[53] C. Song, W. Xu, H. Wu, X. Wang, Q. Gong, C. Liu, J. Liu, L. Zhou, Photodynamic therapy induces autophagy-mediated cell death in human colorectal cancer cells via activation of the ROS/JNK signaling pathway, Cell Death Dis. 11 (2020) 938.
[54] P.H. Chen, J. Wu, C.C. Ding, C.C. Lin, S. Pan, N. Bossa, Y. Xu, W.H. Yang, B. Mathey-Prevot, J.T. Chi, Kinome screen of ferroptosis reveals a novel role of ATM in regulating iron metabolism, Cell Death Differ. 27 (2020) 1008–1022.
[55] N. Yamada, T. Karasawa, H. Kimura, S. Watanabe, T. Komada, R. Kamata, A. Sampilvanjil, J. Ito, K. Nakagawa, H. Kuwata, S. Hara, K. Mizuta, Y. Sakuma, N. Sata, M. Takahashi, Ferroptosis driven by radical oxidation of n-6 polyunsaturated fatty acids mediates acetaminophen-induced acute liver failure, Cell Death Dis. 11 (2020) 144.
[56] A.M. Battaglia, R. Chirillo, I. Aversa, A. Sacco, F. Costanzo, F. Biamonte, Ferroptosis and cancer: mitochondria meet the "iron maiden" cell death, Cells 9 (2020) 1505.
[57] J. Li, J.H. Li, Y.J. Pu, S. Li, W.X. Gao, B. He, PDT-enhanced ferroptosis by a polymer nanoparticle with pH-activated singlet oxygen generation and superb biocompatibility for cancer therapy, Biomacromolecules 22 (2021) 1167–1176.